Impact of AGN on the gas in clusters of galaxies

Fei Xiang

München 13 November 2008

Impact of AGN on the gas in clusters of galaxies

Fei Xiang

Dissertation der Fakultät für Physik
der
Ludwig–Maximilians–Universität München

vorgelegt von Fei Xiang
aus Yunnan, China

München, den 13 November 2008

Erstgutachter: Prof. Dr. Rashid A. SUNYAEV
Zweitgutachter: Dr. Hans BÖHRINGER
Tag der mündlichen Prüfung: 19 December 2008

Contents

Zusammenfassung

Galaxienhaufen sind die grösten durch ihre Eigengravitation gebundenen Systeme im Universum. Ihre Ausdehungen und Massen liegen in den Grössenordnungen von mehreren Megaparsecs bzw. $\sim 10^{14} - 10^{15}$ Sonnenmassen. Haufen entstehen bei der Verschmelzung kleinerer Strukturen; sie existieren im relativ nahen Universum (Rotverschiebungen $z < 1 - 2$). Ihre Hauptbestandteile sind Sterne, heiśes diffuses Gas und dunkle Materie. Sie werden durch das von der dunklen Materie erzeugte Gravitationspotential gebunden. Das heiße diffuse Gas, das sogenannte *Intra-Cluster Medium (ICM)*, stellt den grösten Teil der Baryonen eines Haufens. Dieses Gas hat eine Temperatur von $10^7 \sim 10^8$ K und eine Dichte von $10^{-2} \sim 10^{-4}$ cm^{-3}. Aufgrund der Bremsstrahlung des ICM sind reiche Haufen starke Quellen von Röntgenstrahlung und werden intensiv mittels Röntgenobservatorien untersuchen.

Die Gestalt des ICM steht in direkter Beziehung zum Entwicklungszustand eines Haufens. In einem relaxierten Haufem ist die Verteilung des ICM mehr oder weniger sphärisch symmetrisch. In vielen solcher Haufen findet man einen hellen Zentralbereich bestehend aus relativ kühlem Gas ($T_e \sim 1 - 3$ keV), der durch schrittweise Kühlung und Verdichtung des ICM gebildet wird. Hochaufgelöste Bilder zeigen jedoch darüber hinaus eine vielschichtige Substruktur in den Zentren von Haufen, darunter Phänomene wie Röntgenkavitäten, Kaltfronten (*cold fronts*) und heiße Stellen (*hot spots*). Röntgenkavitäten entstehen bei der Ausdehnung des relativistischen Plasmas der von aktiven Galaxienkernen (*active galactive nuclei, AGN*) ausgesandten Jets im ICM, während Kaltfronten ihren Ursprung vermutlich in der differentiellen Bewegung von Klumpen kühlen und heiśen Gases, etwa nach der Verschmelzung zweier Haufen, haben. Diese Beobachtungen legen eine detaillierte Untersuchung der Hydrodynamik der Zentralgebiete von Haufen nahe.

Eine der offenen Fragen ist die, was mit dem kühlen Gas in einem Haufen passiert. Dieses Gas kann binnen kurzer Zeit ($\sim 10^8$ Jahre) den grösten Teil seiner thermischen Energie durch radiatives Kühlung verlieren. Dennoch beobachtet man keinerlei sehr kaltes (< 1 keV) Gas in den Zentralgebieten reichen Haufen. Eine plausible Erklärung hierfür ist, daś Heizen durch den aktiven Galaxienkern einer zentralen massereichen Galaxie die Kühlung unterbindet. Gewöhnlich vermutet man, daś eine Stośwelle beim Auftreffen des Jets eines AGN auf das umgebende ICM dieses erhitzt und aufbläht. Auf diese Weise entstehen Blasen voller relativistischen Gases (Röntgenkavitäten). Später steigen diese Blasen aufgrund der Auftriebskraft subsonisch im Gravitationspotential des Haufens auf. Während des Aufstiegs dehnen sich die Blasen aus und verrichten am ICM Arbeit. Durch diese Prozesse könnte ein AGN-Jet genug Energie

liefern, um die Temperatur des ICM über 1 keV zu halten. Allerdings weist dieses Bild viele Unsicherheiten auf, etwa hinsichtlich des Anteils der Zeit, während der der AGN aktiv ist, hinsichtlich der thermischen Leitfähigkeit des kühlen Gases, der Mischungsvorgänge im Gas und weiterer Prozesse.

In unserem ersten Projekt (Kapitel 3) wird der Einfluß der thermischen Leitfähigkeit auf eine sich durch heißeres ICM bewegende kalte Gaswolke (Kaltfront) betrachtet. In realen Haufen beobachtet man Kaltfronten als scharfe Sprünge von Oberflächenhelligkeit, Temperatur und Dichte des ICM. Der Sprung (die Grenzschicht) selber ist häufig sehr schmal. In einigen Haufen (z. B. A3667) beträgt die Breite der Grenzfläche weniger als eine mittlere freie Weglänge des Gases. Dies bedeutet, daß Transportprozesse durch die Grenzfläche unterdrückt sind (etwa durch Magnetfelder).

Hier betrachten wir die Entwicklung der Grenzfläche zwischen einer kalten Gaswolke und heißerem Gas, das über diese Wolke hinwegströmt. Aushgehend von den grundlegenden Gleichungen der Hydrodynamik mit Wärmeleitung argumentieren wir, daß es nahe dem Stagnationspunkt der Strömung eine Grenzschicht von konstanter Dicke Δ gibt, wobei Δ von der Größenordnung $\sim \sqrt{kR/U}$ ist; R ist der Krümmungsradius der Wolke, U die Geschwindigkeit der Strömung im Unendlichen, und k die thermische Leitfähigkeit des Gases. Semi-analytische Rechnungen zeigen, daß, selbst wenn sich die anfängliche Dicke der Grenzschicht von Δ unterscheidet, die Entwicklung schnell zu einem nur von k, R und U abhängigen stabilen Wert der Dicke führt. The für die Ausbildung einer stabilen Grenzschicht nötige Zeitdauer ist $\sim R/U$. Diese Argumentation wird bestätigt durch numerische Simulation mit Hilfe eines SPH-Codes. Die Kombination einer analytischen Lösung und numerischer Simulationen erlaubt uns die Ableitung der Dicke der Grenzschicht:

$$\Delta r \approx 40 \left(\frac{\delta}{0.5}\right) f^{0.5} T_5^{5/4} R_{300}^{0.5} U_{1400}^{-0.5} N_{0.002}^{-0.5} \ \mathrm{kpc}, \tag{0.1}$$

wobei der Faktor $\delta \sim 0.5$ allen Abweichungen, die in unseren Näherungen begründet liegen, Rechnung trägt; f ist der Koeffizient, um welchen die Spitzersche Leitfähigkeit unterdrückt wird; $T_5 = \frac{T}{5\,\mathrm{keV}}$, $R_{300} = \frac{R}{300\,\mathrm{kpc}}$, $U_{1400} = \frac{U}{1400\,\mathrm{km\,s^{-1}}}$ und $N_{0.002} = \frac{n_e}{2\times10^{-3}\,\mathrm{cm^{-3}}}$. Über diese Beziehung kann die thermische Leitfähigkeit des ICM einfach aus beobachteten Parametern abgeschätzt werden. Für die Kaltfronten im Haufen A3667 beträgt die Dicke der Grenzschicht ~ 5 kpc, womit sich ein Unterdrückungsfaktor von ~ 0.015 ergibt. Die Entstehungszeit beträgt $\sim 10^8$ Jahre und ist damit wesentlich kürzer als die charakteristische Zeitskala für die Verschmelzung von Haufen (10^9 Jahre). Sobald sich die Schicht ausgebildet hat, verändert sich ihre Dicke nur noch langsam in der Zeit. Da die Wärmeleitung unterdrückt wird, kann die gesamte kalte Wolke in A3667 über einen langen Zeitraum der Verdampfung durch das umgebende heiße ICM widerstehen.

In einem zweiten Projekt haben wir versucht, Bedingungen für die Energetik des AGN in M87 durch die Modellierung der Häufigkeitsprofile des ICM aufzustellen. In

Röntgenspektren von Galaxienhaufen beobachtet man viele Emissionslinien schwerer Elemente. Aus der Messung des Verhältnisses des Flusses in Linien zu demjenigen im Kontinuum kann die Häufigkeit schwerer Elemente bestimmt werden. Die Häufigkeit von Eisen im ICM kann gut abgeschätzt werden aus der Linie, die ein heliumartiges Eisenion bei 6.7 keV besitzt. Eisen wird in Sternen erzeugt und in stellaren Winden und bei Supernova-Explosionen ins ICM freigesetzt. Die sich hieraus ergebende Häufigkeitsverteilung sollte dann die Verteilung des von Sternen in der Galaxie ausgestrahlten Lichtes und die Dichteverteilung des ICM widerspiegeln. Das Häufigkeitsprofil sollte ein ausgeprägtes Maximum bei der cD-Galaxie des Haufens aufweisen. Das beobachtete Eisenhäufigkeitsprofil erscheint jedoch wesentlich breiter. Dies impliziert die Existenz eines wie auch immer gearteten Mechanismus, der Eisen aus den Zentralgebieten des Haufens in dessen äußere Regionen transportiert.

Wenn der Jet eines AGN auf das ICM trifft, wird das Gas in den Zentralgebieten von Haufen aufgeheizt und seine Entropie wächst. Dies führt zu Konvektion im ICM und Gas von hoher Entropie und hoher Elementhäufigkeit strömt vom Zentrum hinaus zu größeren Radien. Wir wandten dieses vereinfachtes Modell auf M87 an. Zuerst berechneten wir das Entropieprofil nach der Ausbreitung einer von einem AGN angetriebenen Stoßwelle (für unterschiedliche Parameter des Ausbruchs, der den Stoß ausgelöst hat). Die sich ergebenden Profile zeigen, daß das Entropieprofil von M87 für eine Energie und eine Dauer des Ausbruchs von $5 \times 10^{56} \sim 5 \times 10^{58}$ erg bzw. $\sim 2 \times 10^5 - 2 \times 10^7$ Jahren invertiert wird. Die Entropie in der zentralen Region ($r < 10$ kpc) wird höher als diejenige in weiter außen liegenden Gebieten. Daher wird das Gas nach größeren Radien hin strömen und schließlich wird sich ein neues, im Radius monotones (nicht fallend) Profil einstellen. Zur selben Zeit bewirken diese Gasbewegungen die Umverteilung schwerer Elemente im Radius.

Die sich einstellenden Profile zeigen, daß ein einziger Stoß die zentrale Häufigkeitsspitze ausschmieren kann und das Gas innerhalb der zentralen ~ 6 kpc durchmischen kann. Im Falle von M87 weist die Häufigkeit keine Spitze im Zentrum auf. Diese Abwesenheit eines sehr starken Häufigkeitspeaks im Zentrum legt nahe, daß der zentrale AGN häufige (im Abstand weniger zehn Megajahre) und eher schwache Ausbrüche erzeugt und nicht seltenere (im Abstand weniger hundert Megajahre) und um eine Größenordnung stärkere. Ein schwacher Stoß, wie er unlängst in Röntgendaten von M87 gefunden wurde, ist allerdings bei weitem zu schwach, um die Häufigkeitsprofile bei größeren Radien zu beeinflußen. Eine mögliche Erklärung der Häufigkeitsprofile in M87 ist, daß die Durchmischung des Gases anstatt durch den Stoß selber durch das Mitreißen von Gas durch aufsteigende Blasen relativistischen Gases angetrieben wird.

Im Bilde von einem AGN getriebenen effizienten Mischens wird die Größe der Region, innerhalb derer das gas durchmischt wird, durch die Energetik des AGN bestimmt, die benötigt wird, ein flaches Entropieprofil zu erreichen. Somit können wir die den Mischungsradius und die Energetik miteinander verknüpfen und die Häufigkeitsprofile als Indikator für diesen Prozess verwenden. Mittels dieser Methode ver-

knüpfen wir die Effizienz der Heizung des Gases und das Mischen der Metalle miteinander. Angewandt auf M87 ergibt sich eine zeitgemittelte Heizleistung des AGN von wenigen 10^{43} ergs/s, was von derselben Grösenordnung ist wie die Energieverluste des Gases durch Strahlung. Dieses Ergebnis unterstützt die Idee, daß das Heizen des Gases durch AGNs in Galaxienhaufen die Kühlungsverluste des Gases ausgleichen kann und gleichzeitig Metalle innerhalb einer Region von $\sim$ 20-100 kpc umverteilen kann.

Die oben beschriebenen Projekte wurden in Zusammenarbeit mit E. Churazov, K. Dolag, V. Springel, A. Vikhlinin, E. Rudometkin, W. Forman und H. Böhringer durchgeführt.

Summary

Clusters of galaxies are the largest self-gravitationally bound systems in the Universe. Their sizes are of order of Megaparsecs and masses $\sim 10^{14} - 10^{15}$ solar masses. The clusters are formed by mergers of smaller structures and they exist in a relatively nearby Universe (redhshifts $z < 1 - 2$). The main components of clusters are stars, hot diffused gas and dark matter. They are bound together in a gravitational well mainly provided by dark matter. Hot diffused gas, also called Intra-Cluster Medium (ICM), is the main constituent of baryons in clusters. This gas has a temperature of $10^7 \sim 10^8$ K and the density of $10^{-2} \sim 10^{-4}$ cm^{-3}. Due to bremsstrahlung radiation from the ICM rich clusters are powerful sources of X-rays and today they are intensively studied by space X-ray observatories.

The ICM morphology is directly related to the cluster evolutionary stage. In a relaxed clusters, the ICM distribution is more or less spherically symmetric. Often in such clusters we see a bright core, made of relatively cool gas ($T_e \sim 1-3$ keV), which is formed by gradual cooling and compression of ICM. But high spatial resolution images also show complex substructure in clusters cores, including such phenomena as X-ray cavities, cold fronts and hot spots. X-ray cavities are formed by the expansion of relativistic plasma from AGN jets in the ICM, while cold fronts are thought to be caused by the differential motions of cool and hot gas lumps (e.g. following a cluster merger). These observations suggest that the hydrodynamics in cluster's central regions needs to be investigated in detail.

An open question is what happens to the cool gas in cluster. This gas can loose most of its thermal energy in short time ($\sim 10^8$ years) because of radiative cooling. However very cold gas (< 1 keV) is not observed in the cores of rich clusters. A plausible explanation is that heating by AGN in a central massive galaxy quenches the gas cooling. Usually it is assumed that when AGN jet encounters the ambient ICM, the shock heats and blows up local ICM. This way bubbles (X-ray cavities) full of relativistic plasma are formed. Later bubbles are lifted subsonically in a gravitational well of a cluster by buoyancy force. When bubbles are rising, they expand and do work on the ICM. Via such process an AGN jet could provide energy to keep ICM temperature above the 1 keV. However there are many uncertainties in this picture, e.g. duty cycle of AGN activity, thermal conductivity in cool gas, gas mixing, etc.

In our first project (Chapter 3) the impact of thermal conduction on a cold gaseous cloud moving through hotter cluster ICM is considered (cold front). In real clusters cold fronts are observed as sharp jumps of the surface brightness, temperature and

density of the ICM. The jump (interface) itself is often very narrow. In some clusters (e.g. A3667), the width of the interface is even smaller than the mean free path in the gas. This implies that the transport processes across the interface are suppressed (perhaps by magnetic fields).

Here we consider an evolution of the interface between a cold gaseous cloud and a hotter gas flowing over the cloud. Starting with the basic hydrodynamics equations with thermal conduction, we argue that near the stagnation point of the flow there is an interface layer with constant thickness Δ, where Δ is of order $\sim \sqrt{kR/U}$, where R is the curvature radius of the cloud, U is the velocity of the flow at infinity, and k is the conductivity of the gas. The semi-analytic calculations show that even if the initial interface width is different from Δ, it will quickly evolve to a stable value which just depend on the k, R and U. The time scale needed to form stable interface is $\sim R/U$. Above arguments are well confirmed by the subsequent SPH numerical simulations. Combining the results of an analytic solution and numerical simulations, we can derive the interface width:

$$\Delta r \approx 40 \left(\frac{\delta}{0.5}\right) f^{0.5} T_5^{5/4} R_{300}^{0.5} U_{1400}^{-0.5} N_{0.002}^{-0.5} \ \mathrm{kpc}, \tag{0.2}$$

where the factor $\delta \sim 0.5$ accounts for all departures introduced by the approximations; f is the coefficient by which the Spitzer thermal conductivity is suppressed; $T_5 = \frac{T}{5\,\mathrm{keV}}$, $R_{300} = \frac{R}{300\,\mathrm{kpc}}$, $U_{1400} = \frac{U}{1400\,\mathrm{km\,s^{-1}}}$, and $N_{0.002} = \frac{n_e}{2\times10^{-3}\,\mathrm{cm^{-3}}}$. By this relation the effective thermal conductivity in ICM could be easily estimated based on observed parameters. For the cold front in cluster A3667, the interface width is ~ 5 kpc, so the suppression factor f is ~ 0.015. The formation time is $\sim 10^8$ years, which is much shorter than the characteristic time scale for cluster merger (10^9 years). Once the layer is formed, its thickness only slowly varies with time. Because thermal conductivity is suppressed, the whole cold cloud in A3667 could persist for a long time against the evaporation by ambient hot ICM.

In a second project we tried to constrain AGN energetics in M87 galaxy through the modeling of the ICM abundance profile. In X-ray spectra of clusters many emission lines from heavy elements are observed. By measuring the ratio of line fluxes to continuum the abundance of heavy elements can be determined. E.g. the abundance of iron in ICM can be well estimated through the 6.7 keV line of He-like iron. Iron is produced in stars and released into ICM by stellar wind and supernova explosion. The resulting abundance distribution should then reflect the distribution of optical light from stars in the galaxy and the ICM density distribution. Such abundance profile should be highly peaked at the cluster's cD galaxy. But in observations the iron abundance profile appears much broader. This implies the existence of some mechanism which transports iron from cluster center to outer regions.

In central regions of clusters, when jet from AGN encounters the ICM, the gas is heated and its entropy increases. This causes convection in ICM and high entropy, high abundance gas moves from the core to larger radii. We applied this toy model

to M87. First, we calculated the gas entropy profile after the propagation of an AGN driven shock (for different parameters of an outburst which caused the shock). The resulting profile show that for the outburst energy of $5 \times 10^{56} \sim 5 \times 10^{58}$ ergs and the outburst duration $\sim 2 \times 10^5 - 2 \times 10^7$ years the M87 entropy profile will be inverted. Entropy in the central region ($r < 10$ kpc) will become higher than further out. So the central gas will move to larger radii and eventually new profile will be formed with the monotonic (non-decreasing with radius) gas entropy. At the same time these gas motions cause redistribution of heavy elements over radius.

The resulting profiles show that a single shock can smeared out the central abundance peak and mix the gas within central $\sim$ 6 kpc region. For M87, its central abundance is not peaked. So the absence of a very strong abundance peak at the very center of M87 suggests that the central AGN produces frequent (every few 10 Myr) and relatively weak outbursts, rather than rarer (every few 100 Myr) and an order of magnitude more powerful events. However a weak shock, recently found in M87 X-ray data, is by far too weak to affect the abundance profile at larger radii. A possible explanation for the M87 abundance profile is that the gas mixing is driven by the entrainment of the gas by buoyant bubbles of relativistic plasma, rather than by the shock itself.

In a picture of efficient mixing driven by an AGN, the size of the region where the gas is mixed is set by the energetic of the AGN, needed to make a flat entropy profile. So we can link the mixing radius and energetics and use abundance profile as a proxy for this process. By this method, we link the gas heating efficiency and metal mixing together. Applied to M87, the derived time-averaged AGN heating power is few 10^{43} ergs/s, which is of the the same order as the gas radiative cooling losses. This result supports the idea that the gas heating by AGNs in clusters can compensate the gas cooling losses and at the same time redistribute metals through the $\sim$20-100 kpc region.

Above projects have been done in collaboration with E. Churazov, K. Dolag, V. Springel, A. Vikhlinin, E. Rudometkin, W. Forman and H. Böhringer.

1 Introduction

Abstract
In this chapter we provide the relevant background for this thesis.

Clusters of galaxies with masses up to few 10^{15} $M_{\odot}$ are the largest gravitationally bound objects in the Universe. According to the widely accepted hierarchical model of structure formation the largest structures are formed by mergers of smaller (less massive) objects. Massive clusters are therefore expected to appear in the Universe only "recently" (redhshifts $z < 1 - 2$) and their number is very sensitive to the cosmological parameters, such the amplitude of primordial fluctuations and dynamics of the Universe expansion which is in turn related to dark energy and dark matter content of the Universe.

Three major constituents make a galaxy cluster: stars (readily observable in bright optical galaxies), hot X-ray emitting gas (observed with modern X-ray space observatories) and dark matter (indirectly observed through its influence on galaxies and gas). It is believed that in clusters the mass fractions of baryons (stars and gas) and the dark matter are representative for the Universe as a whole. Stars is the least massive component out of three, making only few % of the cluster mass, while hot gas and dark matter account for 10%-15% and $\sim 75\%$ respectively. Since the dark matter can not be seen directly we have to use other components to determine main parameters of a cluster (such as e.g. total mass). In particular instrumental are X-ray observations of the hot gas, which are used to accurately map the mass profile of a cluster. This hot gas is a fully ionized plasma with the temperature of tens of millions degrees and the density $10^{-2} - 10^{-4}$ particles per cm^3, which emits radiation primarily through bremsstrahlung and excitation/recombination lines of heavy elements.

While we are confident that the parameters of clusters determined from optical and X-ray data are broadly correct, there are a number observed phenomena in galaxy clusters which are yet to be explained and a number of parameters yet to be measured. For instance we do not fully understand if radiative cooling of the gas in the central regions of clusters is compensated by some sources of energy (e.g. from the activity of supermassive black holes). We also do not know what are the values of such fundamental characteristic of the cluster plasma as thermal conductivity or viscosity. In our research we discuss two simple theoretical models aimed at:

- evaluating thermal conductivity in the gas using X-ray observations of sharp

features in the surface brightness distribution of X-ray emission (so called "cold fronts")

- estimating the energetics of the feedback from the supermassive black holes through its influence on the distribution of heavy elements in the hot gas.

The background about cluster and the related phenomena to our model will be introduced as below in detail.

1.1 Observations of cluster of galaxies

1.1.1 Optical observations

Cluster of galaxies were first found in optical observations as high density of galaxies in small areas on the sky (Wolf, 1906) (e.g. Fig 1.1 right). First catalogues of clusters were established by calculating the number of galaxies within given area. E.g. Abell (1958) is a wildly used catalogue of clusters. Its criteria is as the follows: at least 50 galaxies whose magnitude range m_3 to $m_3 + 2$ are located in a circle of radius $R_A == 1.7/z$ arc minutes, where m_3 is the magnitude of the third brightest galaxy and z is the cluster redshift estimated from these galaxies. The red shift of cluster in Abell catalogue is $(0.02 \leq z \leq 0.20)$. In the past mainly the low redshift clusters were studied because of the limitations of the existing telescopes.

Today many more catalogs of clusters exist, many of them containing clusters with much larger redshifts than were present in Abell catalog.

1.1.2 X-ray observations

X-ray emission of a cluster was observed at first in 1966 (Byram et al. 1966). First X-ray observations of galaxy clusters were carried out by instruments on rockets and balloon. The major advance in X-ray studies came with the Uhuru satellite the first x-ray observatory in space, which made a complete survey of the sky in X-rays and showed that clusters of galaxies are bright extragalactic X-ray sources with luminosity $\sim 10^{43} - 10^{45} erg/s$. In 1978 Einstein observatory became the first imaging X-ray observatory which had the sensitivity orders of magnitude higher than that for any previous X-ray detector. Einstein observatory produced new major surveys of X-ray emission from clusters. Today we have two major operating X-ray observatories in space - XMM-Newton(Fig 1.2) and Chandra(Fig 1.3). They have much better angular and energy resolution than previous observatories. The main instruments on Chandra are 'Advanced CCD Imaging Spectrometer(ACIS)', 'High Resolution Camera(HRC)', 'High Energy Transmission Grating(HETG)', 'Low Energy Transmission Grating(LETG)'. And the X-ray instruments on XMM are 'European Photon Imaging Camera(EPIC)' including 'Metal Oxide Semi-conductor

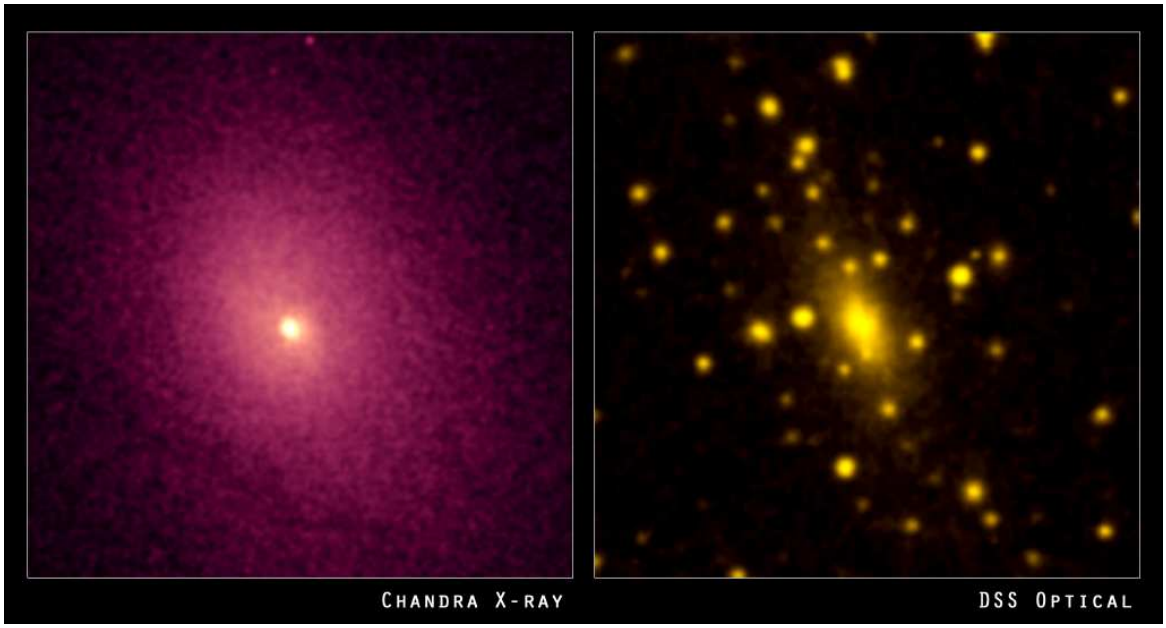

Figure 1.1: X-ray(left) and optical(right) images of cluster Abell 2029(X-ray: NASA/CXC/UCI/A.Lewis et al. Optical: Pal.Obs. DSS, scale:4 arcmin on a side)

Table 1.1: XMM Instruments Performance

instruments	MOS	pn	RGS
Energy Range	$0.15 \sim 12kev$	$0.15 \sim 15kev$	$0.35 \sim 2.5kev$
Sensitivity	10^{-14} [a]	10^{-14} [a]	8×10^{-5}
Field Of View	30'	30'	5'
Angular resolution	6"	5"	-
Time resolution	1.5ms	0.03 ms	16 ms
Spectral resolutionΔE	70 eV	80 eV	1.25 ev [c]

[a] unit:$ergs^{-1}cm^{-2}$
[b] unit:$countss^{-1}cm^{-2}keV^{-1}$
[c] at 0.5 keV

CCD arrays(MOS)' and 'pn CCDs(pn)' and 'Reflection Grating Spectrometer(RGS)'. Their properties are as follows (Strüder et al. 2001, Turner et al. 2001, den Herder et al. 2001,http:// xmm.esac.esa.int; http:// www.chandra.harvard.edu):

X-ray emission in cluster is due to hot diffuse gas (with temperature $10^7K \sim 10^8K$). This hot gas contains main fraction of baryons in cluster. It is also called Intra-Cluster Medium (ICM). The spatial distribution of hot gas reflect the gravitational potential of the cluster and is also connected with the evolution of the cluster.

Table 1.2: Chandra Instruments Performance

instruments	ACIS	HRC	HETG	LETG
Energy Range	$0.2 \sim 10kev$	$0.1 \sim 10kev$	$0.5 \sim 10kev$	$0.08 \sim 6nm$
Sensitivity	4×10^{-15} [a]	4×10^{-15} [a]	-	-
Field Of View	1°	31'	-	-
Angular resolution	0.5"	0.5"	-	-
Time resolution	-	$16\mu s$	-	-
Spectral resolution$E/\Delta E$	$20 \sim 50$	-	$60 \sim 1000$	$30 \sim 2000$

[a] unit:$ergs^{-1}cm^{-2}$ in 10^5s

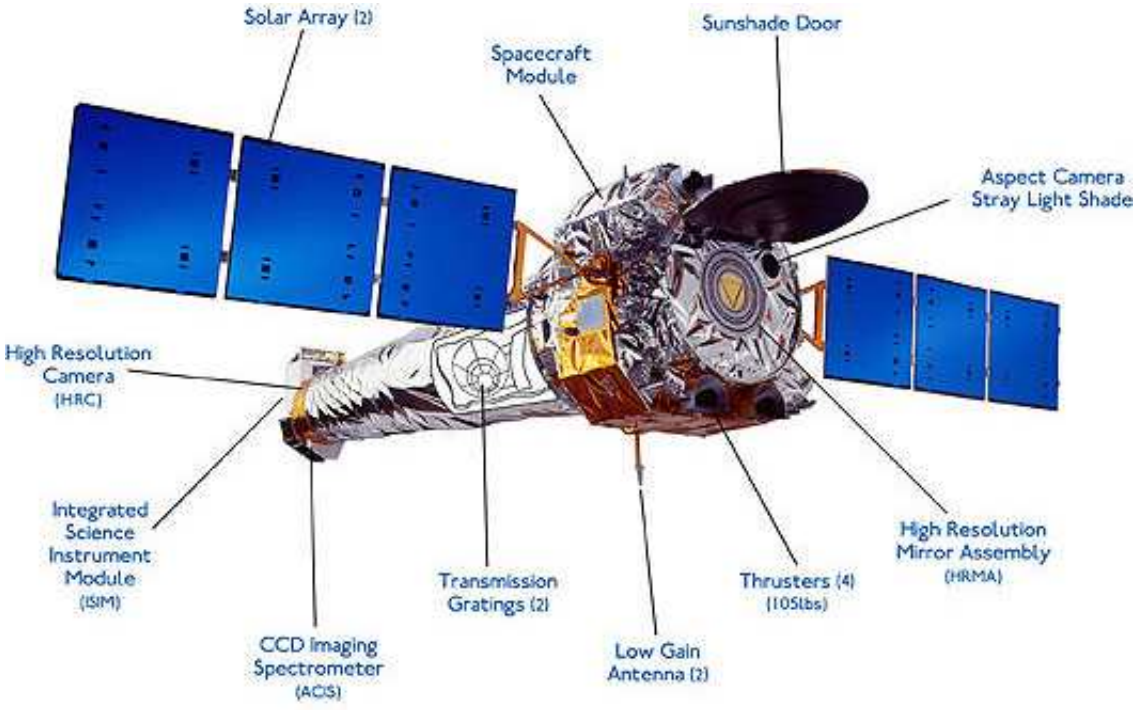

Figure 1.2: The Chandra image(http:// chandra.harvard.edu/ resources/ illustrations/ art_illus1.html)

The X-ray images show directly the ICM's density distribution in a cluster.

Another kind of information that X-ray data provide is spectra (e.g. Fig1.4). X-ray spectra of clusters include the continuum and emission lines. The continuum can be well fitted by an optically thin bremsstrahlung emission model (Mushotzky et al. 1978). The emissivity of bremsstrahlung is:

$$\varepsilon^{ff} = \frac{2^5\pi e^6}{3m_e c^3}(\frac{2\pi}{3m_e k})^{1/2} z^2 n_e n_i g_{ff}(z, T_g, \nu) T_g^{-1/2} exp(-\frac{h\nu}{kT_g}) \tag{1.1}$$

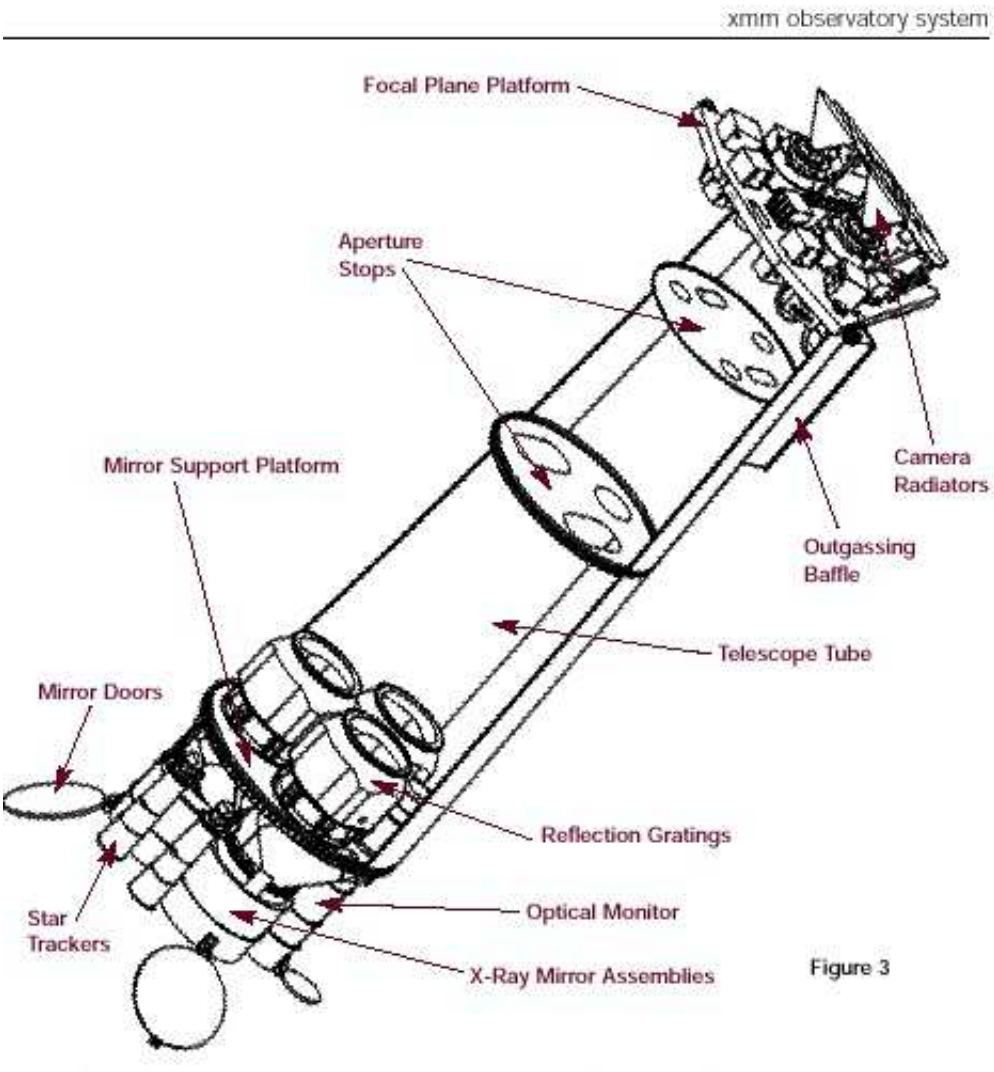

Figure 1.3: The XMM structure(http:// xmm.esac.esa.int/ external/ xmm_user_support/ documentation/ technical/ Spacecraft/ index.shtml)

Here the T_g is gas temperature; n_e and n_i are the number densities of electrons and ions respectively; z is the charge of the ion and g_{ff} is Gaunt factor, which is of order of ~ 1, h is the Plank constant, ν is the frequency of x-ray emission, k is the Boltzmann constant. Through spectra fitting, the properties of ICM can be determined such as temperature, density and abundance of heavy elements (Mitchell et al. 1979, Sarazin & Bahcall 1977).

In addition to the continuum, bright emission lines are observed in cluster's x-ray spectra. The $'7keV$ Fe line was observed first in 1976 (Mitchell et al. 1976) and identified with the k_α line of strongly ionized iron. Nowadays the k_α lines of the O,

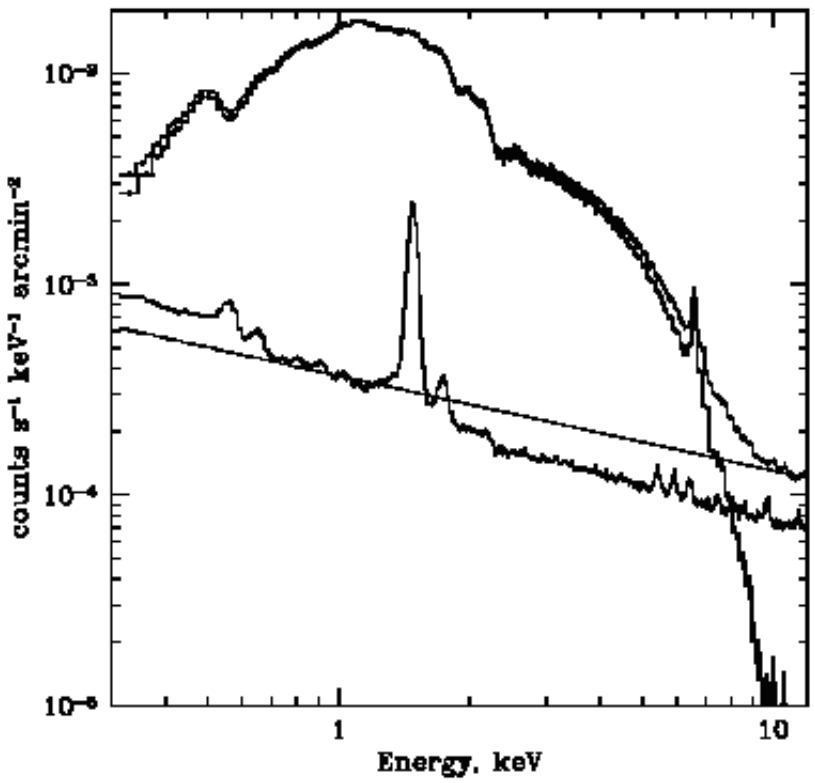

Figure 1.4: X-ray spectrum of the Perseus cluster

Mg, Si, S, Ar, Ca, Fe and k_β are observed (Fig 1.5). Emission lines could provide detailed information on ICM properties. E.g., By lines' redshift, the redshift of clusters could be measured. The cluster RX J1053.7+5735 is the first cluster whose red shift($z = 1.14$) measured in X-rays before it was obtained from optical data (Hashimoto et al. 2004). Ratio of lines' strength is a useful indicator of a plasma temperature and of the presence of multi-temperature components. In particular, the existence of a cool gas ($T \sim 10^5 K$) was ruled out by line fitting in some clusters (Peterson et al. 2003) (Fig 1.6).

1.1.3 Radio observations

Radio emission of galaxy cluster mainly comes from the synchrotron radiation of relativistic electrons (10^9 keV) in clusters' magnetic field $\sim \mu Gauss$ (Miley 1980). Typically measured frequency is around GHz and flux is 100 $\sim$ 1000 mJy corresponding to the magnetic field μGauss(Miley 1980). The radio spectra are power laws: $I_\nu \propto \nu^{-\alpha}$, which means the energy spectrum of relativistic electrons also is a power law. The radio spectra in clusters are usually steep ($alpha > 1$) (McHardy 1979). By assuming an energy equi-partition between magnetic fields and relativis-

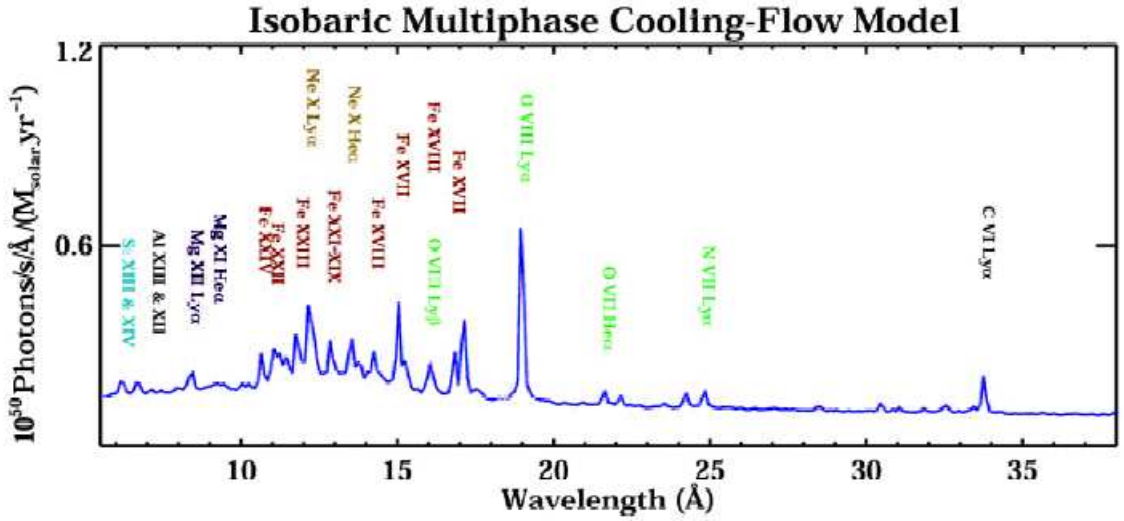

Figure 1.5: The emission lines predicted in isobaric multi-phase cooling flow model. The assumed maximum temperature is 6keV and abundance is 1/3 solar value (Peterson et al. 2003)

tic plasma, the magnetic field B_{me} and the minimum energy density (u_{me}) can be inferred by following formula (e.g. Miley 1980):

$$B_{me} = 5.69 \times 10^{-5} [\frac{1+k}{\eta}(1+z)^{3-\alpha}\frac{1}{\theta_x \theta_y s sin^{3/2}\phi} \times \frac{F_0}{\nu_0}\frac{v_2^{\alpha+1/2} - v_1^{\alpha+1/2}}{\alpha+1/2}]^{2/7} gauss \quad (1.2)$$

$$u_{me} = \frac{7}{3}\frac{B_{me}^2}{8\pi} = 0.0928 B_{me} ergcm^{-3} \quad (1.3)$$

Here k is the energy ratio between ions and electrons; η is the local filling factor of relativistic plasma; z is the redshift; α is spectral index; θ_x and θ_y (arcsec) is the source size; s(kpc) is the thickness along the line of sight; ϕ is the angle between the magnetic field and the line of sight; $\langle sin^{-3/7}\phi \rangle \sim 1.5$; F_0(Jy) is the brightness at frequency ν_0(GHz), ν_1 and ν_2(GHz) are the upper and lower cut off frequencies presumed for the radio spectrum.

In above formula some important parameters such as threshold of energy spectra and the energy of relativistic heavy particles can not be obtained from radio observation. To get complete properties, it is necessary to combine radio observation with the hard x-ray observation (e.g. Pfrommer & Enßlin 2004, Petrosian 2004), which originates from the inverse Compton scattering between relativistic particles and cosmic micro-wave background (CMB) (e.g. Nevalainen et al. 2004).

Radio sources in clusters could be compact or extended. The compact sources have compact cores ($< 2kpc$) and are directly associate with the galaxies in clusters. The jets from Active Galaxy Nuclei (AGN) are responsible for compact sources. If the host galaxy is moving rapidly in ICM, the jet will be distorted when interacting

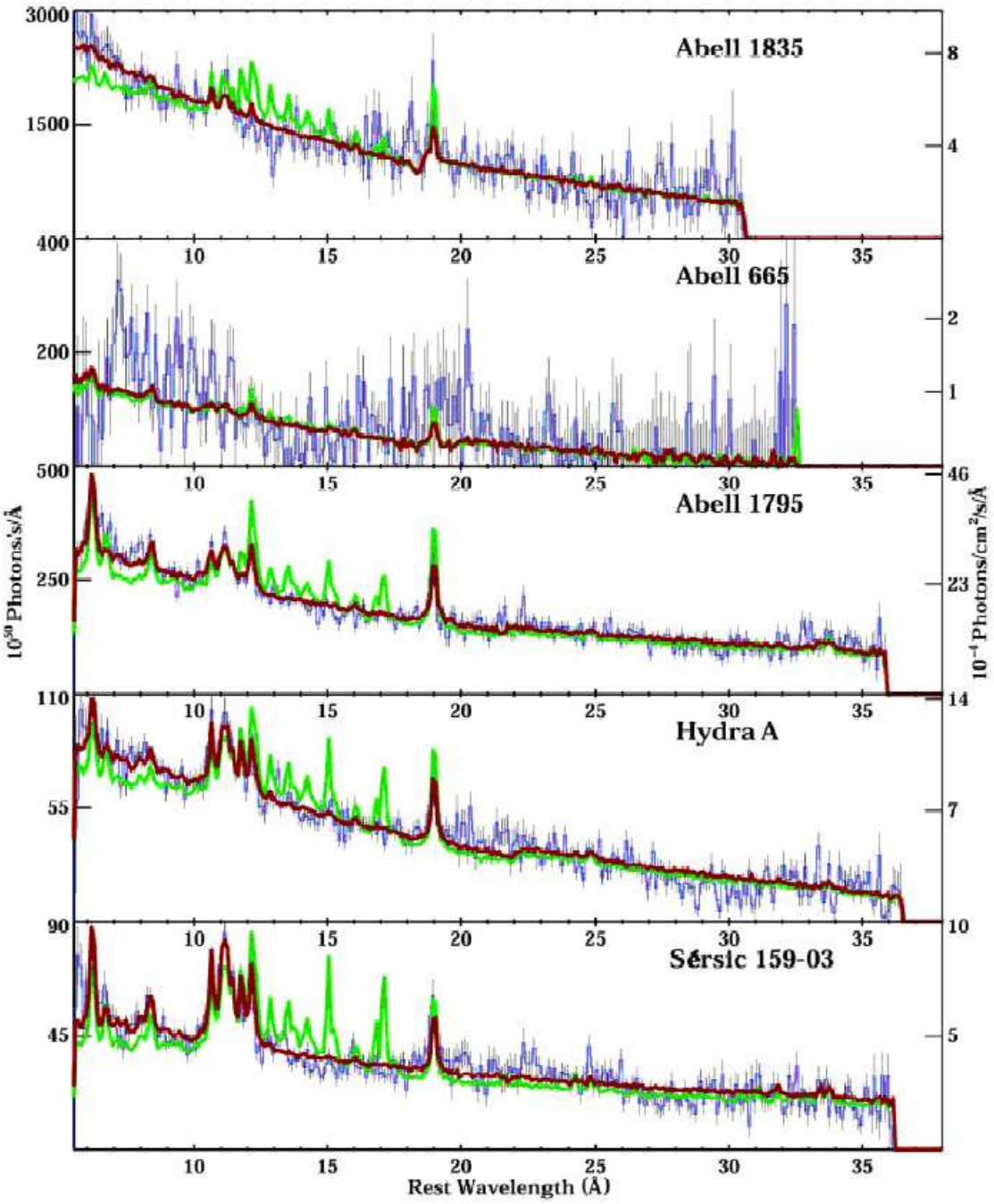

Figure 1.6: Comparison between X-ray spectra of the XMM-Newton RGS'data (blue), the empirical best fit model (red) and cooling flow model (green). The figure reveals that in cooling flow model the emission lines from the component with lowest temperature will be over-produced. (Peterson et al. 2003)

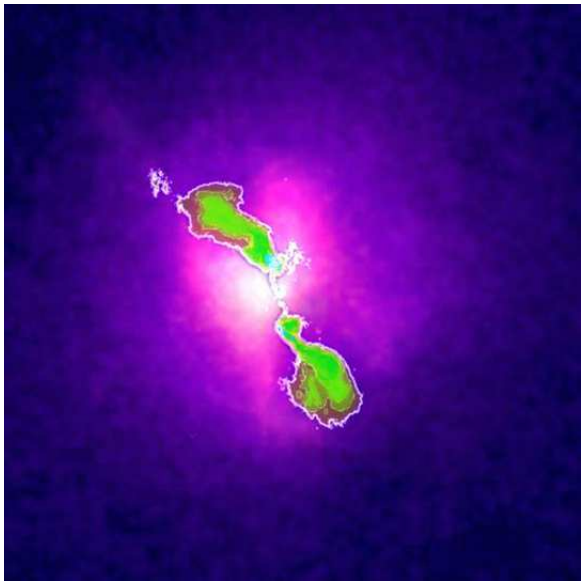

Figure 1.7: The radio image (green and maroon) of Hydra A cluster is superposed on its Chandra X-ray image (pink, and blue. Credit: X-ray: NASA/CXC/SAO; Radio: NRAO

with ICM. These sources are called "head-tail". Provided that the density of ICM is known through the x-ray observation, the velocity of galaxy can be estimated (e.g. Miley et al. 1972).

The extended source can be classified as radio lobe (Fig 1.7) and radio halo (Fig 1.8). Radio lobes are usually connected by jets with an AGN. They are formed by relativistic plasma of jets expanding in ICM (e.g.Miley 1980). In Chandra and XMM's x-ray images, x-ray dark regions (cavities) have been found to overlap with the radio lobes, e.g. in Perseus (Fabian et al. 2002), Hydra A (Fig 1.7, McNamara et al. 2000).

A radio halo is much larger than radio lobe but less bright (e.g. Hanisch 1982). In X-ray observations, the cluster with a radio halo has often signs of a recent merger, e.g. disturbed appearance or double component in center (e.g. Govoni et al. 2004). So the radio halos are thought to originate from the clusters' merger. The relativistic particles are thought to be accelerated by merger shock and turbulence.

1.2 Cluster's mass

There are several ways to estimate the mass of a cluster from observation. From optical observation, the velocity dispersion of member galaxies can be measured.

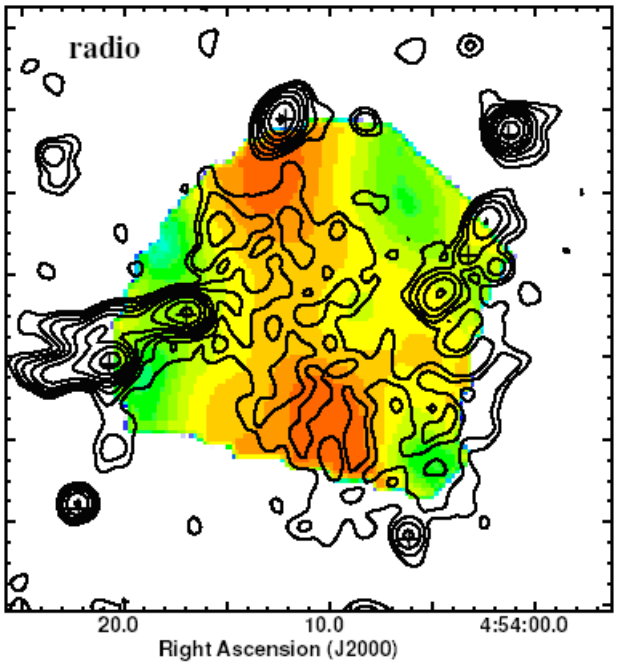

Figure 1.8: Chandra temperature map(color) overlaid with radio contours for cluster A520 (Markevitch et al. 2005).

Then the total mass of the cluster can be estimated though the following:

$$M_{tot} = \frac{3R_G\sigma_r^2}{G} = 7 \times 10^{14} M_\odot \left(\frac{\sigma_r}{1000 km/s}\right)^2 \left(\frac{R_G}{Mpc}\right) \tag{1.4}$$

Here, $R_G \sim 1Mpc$ and could be estimate from radius including most of galaxies (Limber & Mathews 1960), $\sigma_r = \langle (v_r - \langle v_r \rangle)^2 \rangle^{\frac{1}{2}}$ is the radial velocity dispersion of galaxies and G is the gravitational constant. M_{tot} of a rich cluster is $\sim 10^{15} M_\odot$ and the optical luminosity of clusters is $\sim 10^{13} L_\odot$. The ratio of mass to luminosity is $\sim 100 M_\odot/L_\odot$, which is a hundred times that of star and tens of times that of galaxies (Faber & Gallagher 1979). The mass-luminosity ratio implies that large part of content in cluster is optically invisible. Gravitational lensing is another useful method to measure the cluster mass using optical observations.

Another way to calculate a cluster mass is through X-ray observations. When assuming that the ICM is in the hydrostatic equilibrium between pressure gradient and gravity, the cluster's mass distribution can be measured by following (e.g. Fabricant et al. 1980):

$$M_{tot}(< r) = -\frac{k_B T r^2}{G\mu m_p} \left(\frac{d(ln(n_e))}{dr} + \frac{d(ln(T))}{dr}\right) \tag{1.5}$$

M_{tot}, n_e, T are the total mass within the radius(r), the number density of electrons and the temperature respectively. The results from all three methods often agree

at large radii, but sometimes disagree in the centers (e.g. Miralda-Escude & Babul 1995, Wu & Fang 1997). The reason of this difference is not clear. The high spatial resolution observations of Chandra and XMM indicate that the structure of cluster center is more complicate than the spherical symmetry. In cluster's centers exist the x-ray cavities, cold cloud, hot spot and so on. So the hydrodynamics there need to be investigated in detail.

1.3 Formation of clusters

In the scenario of cosmic hierarchical structure formation e.g. Press & Schechter 1974), the cosmic structure originated from the growth of fluctuations in dark matter. Initially the dark matter distribution is almost uniform, but with small fluctuations of over-density ($\frac{\triangle\rho}{\rho} \sim 10^{-5}$ at scales of degrees at a redshift $z \sim 1000$). Due to gravity these fluctuations grow bigger and bigger, become nonlinear and form virialized dark matter halos. The mass of dark matter halo is determined by length scale of fluctuations. The mass of cluster is $\sim 10^{15} M_{\odot}$ and correspondingly comes from the fluctuations of several Mpc. The baryons, after decoupling from the photons, will fall into gravitational well provided by dark halo. With the release of gravitational energy, the gas will be heated to $10^7 \sim 10^8$K. In smaller dark halos the gas cools and form stars (i.e. galaxies). These galaxies also fall to the cluster potential well. So in optical observation we can found the galaxies clustered in several Mpc. Numerical simulations of recent years have represented such a scenario(Springel et al. 2005a, Springel 2005b, Borgani et al. 2004)(Fig1.9, Fig1.10).

After the cluster is formed, the evolution of the ICM remains complex. The ICM will sink to cluster center if the gas is able to cool (e.g. Fabian 1994). The evolution of cluster galaxies also are coupled with the evolution of cluster. The AGN, star formation and so on in galaxies can provide energy to prevent ICM cooling. The activities in clusters such as cluster merger can impact on the star formation in galaxies. Various of hydro-dynamical phenomena appear in this stage.

1.4 Properties of ICM

The main content of baryons in cluster is ICM, accounting for 90% of all baryons (David et al. 1990). For the hot gas, the X-ray luminosity is $10^{43} \sim 10^{45} erg/s$, the temperature is $10^7 \sim 10^8$K and density is $10^{-2} \sim 10^{-4}/cm^3$. At large scales, the X-ray images of clusters are often relatively symmetric. It's often assumed that the cluster is spherically symmetric or at least has ellipsoidal shape. Often the brightness, temperature and density profiles with radius are used to characterize the properties of ICM.

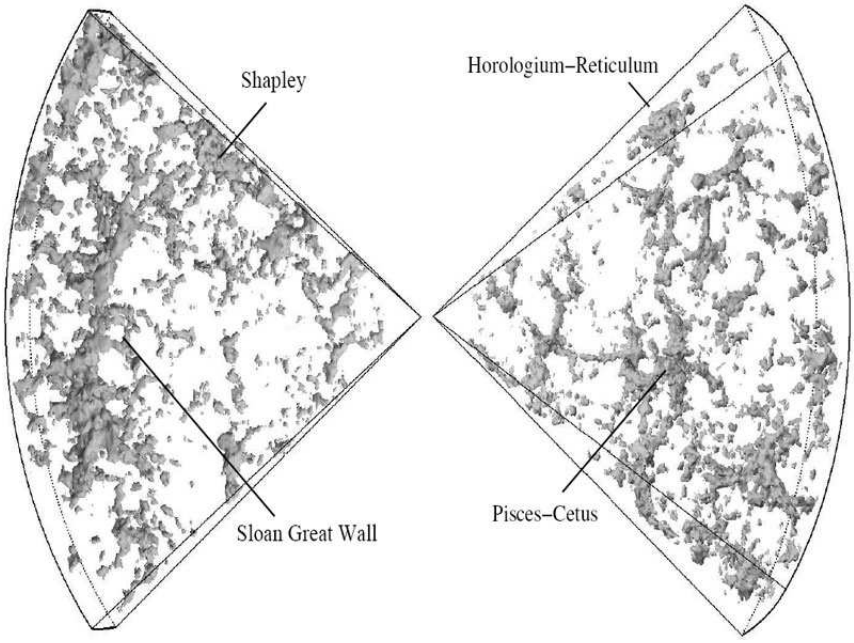

Figure 1.9: The largest structures discovered in 2DF galaxy survey (W. Schaap et al., 2dF Galaxy Redshift Survey, scale:redshift $z \leq 0.1$)

1.4.1 X-ray brightness distribution

The spatial distribution of projected brightness with radius in cluster can be well fit by a β model:

$$I(R) = I_c \left(1 + \left(\frac{R}{r_c}\right)^2\right)^{-3\beta+\frac{1}{2}} \tag{1.6}$$

Although β model performs well in many cases, for some cluster with specially high central brightness the double *beta* model is necessary:

$$I(R) = I_1 \left(1 + \left(\frac{R}{r_1}\right)^2\right)^{-3\beta_1+\frac{1}{2}} + I_2 \left(1 + \left(\frac{R}{r_2}\right)^2\right)^{-3\beta_2+\frac{1}{2}}. \tag{1.7}$$

This model is especially useful when dealing with cool core clusters, having a peak of the surface brightness in the center (Fig 1.11).

From X-ray observations clusters can be divided into two classes by brightness distribution : regular and irregular (Forman & Jones 1982, Jones & Forman 1984). In irregular cluster the spatial distribution of X-ray brightness has several peaks. The irregular clusters are considered as dynamically young and not relaxed. A regular cluster (e.g. Fig 1.1(left)) shows simpler morphology. The brightness distribution is smooth and has a strong peak in center. The regular cluster also has high X-ray

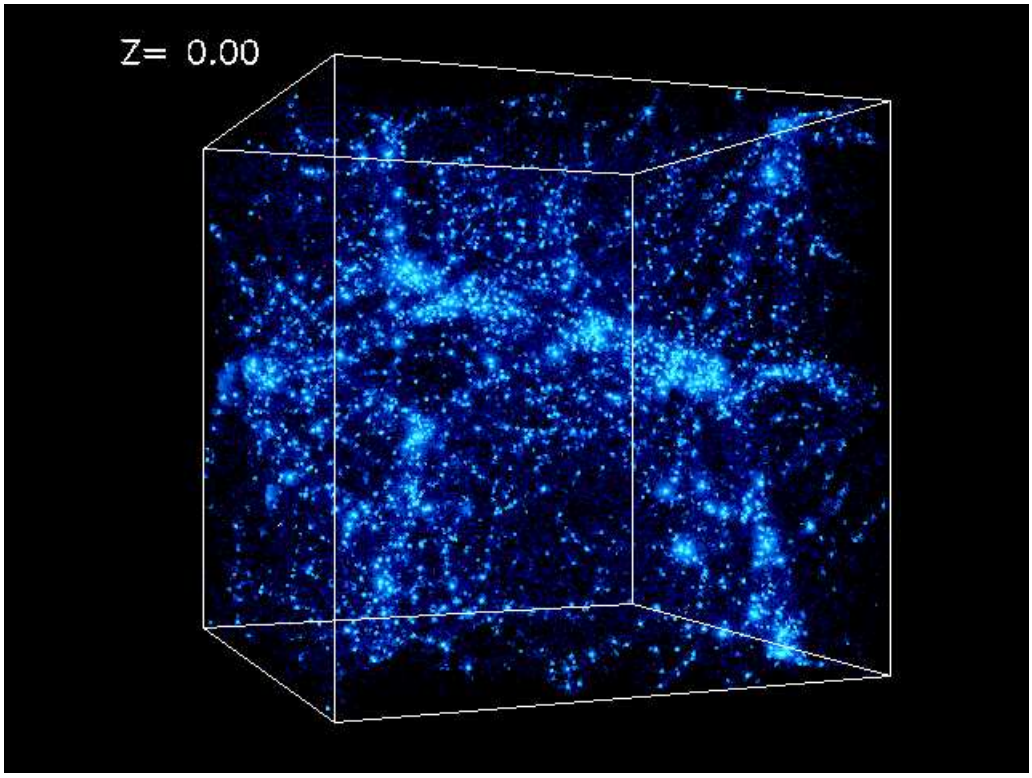

Figure 1.10: The large-scale filaments produced in numerical simulation: The simulation is performed in a model with cold dark matter and dark energy (Ω_M = 30%,Ω_Λ = 70%). The box size is 43 Mpc. The simulation begins at redshift z is 30 and the large scale structure does not change much after $z \sim 0.5$. (Simulations were performed at the National Center for Supercomputer Applications by Andrey Kravtsov (The University of Chicago) and Anatoly Klypin (New Mexico State University). Visualizations by Andrey Kravtsov.)

luminosity, temperature and galaxy velocity dispersion. The fraction of spiral galaxy in regular cluster is lower (Bahcall 1977).

1.4.2 Cool core clusters

According to the temperature and density distributions in central regions, clusters can also be classified into clusters with 'cool core' (Fig 1.13 left) or without 'cool core'(Fig 1.13 right). The clusters without 'cool core' have a relative flat temperature and density distribution in the center. The 'cool core' clusters have instead a dense and cool gas in center(Fig 1.14). In X-rays cool core clusters show a strong central peak of the surface brightness brightness (Fig 1.1 left). The brightest cluster galaxy (BCG) usually lies very close to the location of the peak in the X-ray surface brightness distribution.

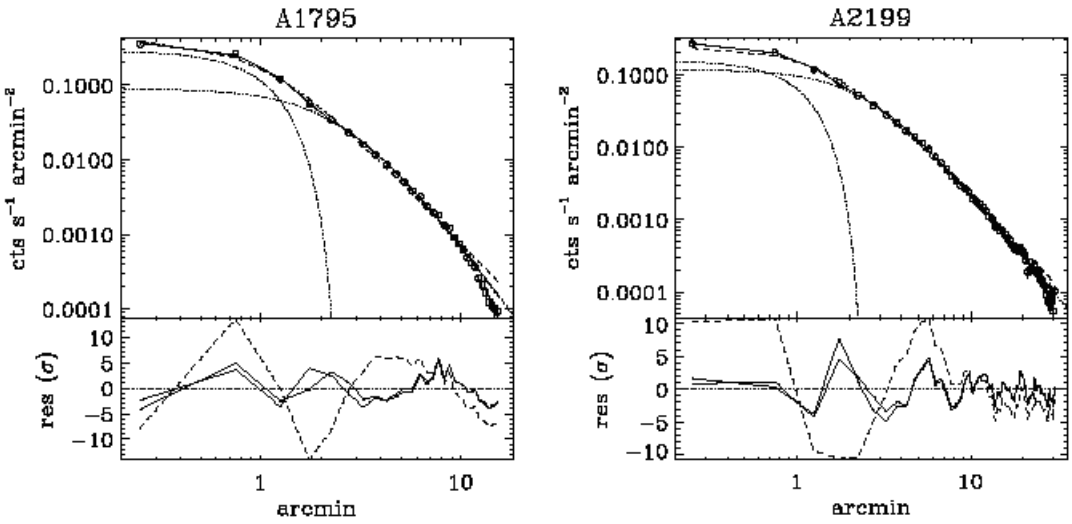

Figure 1.11: The examples of cluster's brightness distribution fitted with β model and double β model. The single β model: dashed line; the double β model: solid line. The dotted lines show the two component of the double β models.(Ettori 2000)

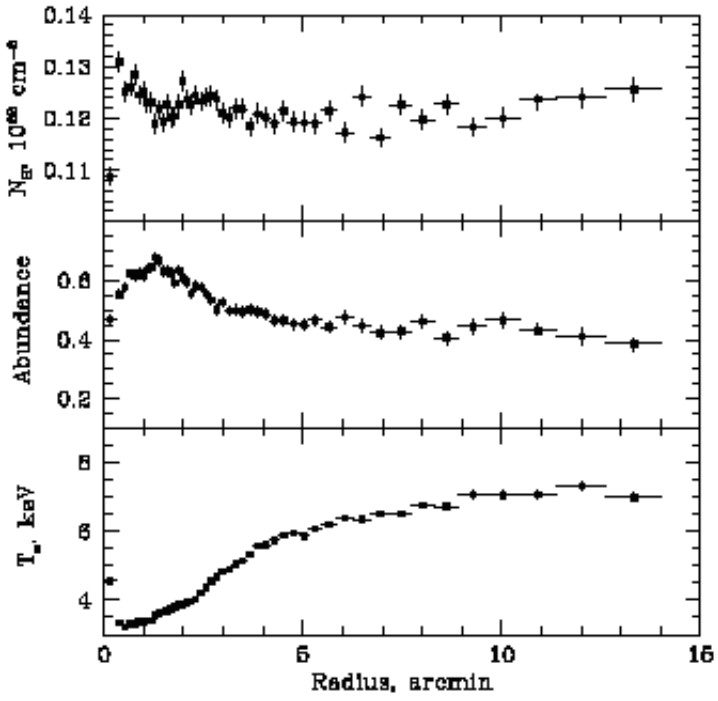

Figure 1.12: The density, temperature and abundance distributions in the Perseus cluster. (Churazov et al. 2003)

The cool gas in the center of cool core clusters could appear due to the ICM radiative cooling. A model of a 'cooling flow' was developed to describe a process of gradual gas cooling in a cluster potential (e.g. Fabian,1994). The radiation mechanism in ICM is thermal bremsstrahlung, so the emitting power per volume is $j(T, n_e) \sim 2.4 \times 10^{-27} T^{-1/2} n_e^2 \; erg/s/cm^3$, where T is temperature and n_e is electron density (e.g. Raymond et al. 1976). The cooling time for ICM can be written as $\frac{3n_t k_B T}{2j(T,n_e)}$, where n_t is total particle density of ICM. For the typical ICM parameters in the cool core clusters the cooling time is of order $10^8 - 10^9$ years. In the cooling flow model the gas cools and sinks to cluster central region. The model predicts the existence of a cool/warm gas ($< 10^6$K) in very center of a cluster. But recent observations place tight limits on the presence of such gas (e.g. Peterson et al. 2003)(Fig 1.6). So some source of energy is thought to be present in cluster centers to prevent gas from cooling to low temperatures. The most popular model today is heating due to AGN activity, although details of this process are not yet well understood.

1.4.3 The distribution of iron in ICM

The iron in the ICM is detected through the iron X-ray emission lines (in particular 6.7 keV line of He-like iron) in the clusters' X-ray spectra. The spatial distribution of iron in cluster can be derived through spectra fitting for different regions, e.g.(Sanders et al. 2004)(Fig 1.15). The 6.7 keV line is so bright that iron distribution is often measured with higher precision than the distribution of other elements. It is found that the distribution of iron depends on the cluster type: in cluster without a cool core, the distribution of iron is flat (Fig 1.16); in cluster with a cool core, there is a central abundance peak of Fe abundance up to 1.5-2 solar (De Grandi & Molendi 2001, Böhringer et al. 2004) (Fig 1.17).

The iron is produced by various stellar generations in cluster and released by supernova explosions and stellar winds. From the distribution of iron and other elements (O, Mg) with radius one can evaluate the role of various mechanisms for enrichment of the ICM. Using the notion that O, Mg are produced by SN II, while iron is produced effectively by SNIa it was found that in out region of cluster heavy elements are mainly produced by SN II; in inner region the SN II's contribution only amounts to 10% and the rest is mainly produced by SN Ia (e.g. Finoguenov et al. 2002).

The production of iron in the centers of cool core clusters is believed to be due to the central cluster galaxy. Therefore the distribution of produced iron should follow the optical light distribution in cluster, which is highly peaked at the central galaxy. The transportation of produced iron could be due to the gas motions. For none cooling core cluster, a recently merger could cause a uniform mixing of iron up to a large distance from the center. For a cooling core clusters, Böhringer(2004) inferred that several $Gyears$ are needed to form the central abundance peak in these clusters.

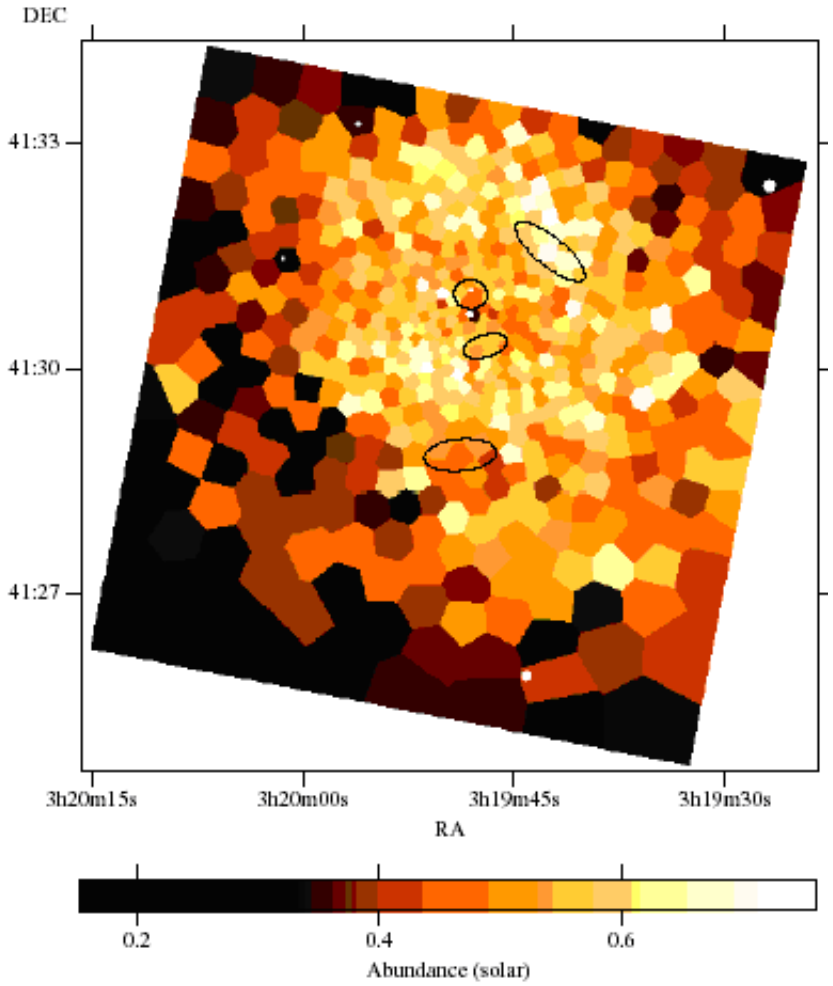

Figure 1.13: The abundance map of Perseus cluster. The uncertainty is 0.04 solar abundance in the center and 0.08 solar abundance in outer region (Sanders et al. 2004)

This requires that the cluster didn't experience a merger during this period. However the observed width of the abundance distribution is is much broader than optical light peak in cluster. This point can be explain well by diffusion of iron caused by stochastic gas motions in ICM (Rebusco et.al 2005, 2006). Recent observations also revealed that the high abundance gas is accompanied with the AGN jet in cluster M87 (Simionescu et al. 2008). In this Thesis we describe a simple model of iron transportation in the ICM due to gas motions induce by AGN jets.

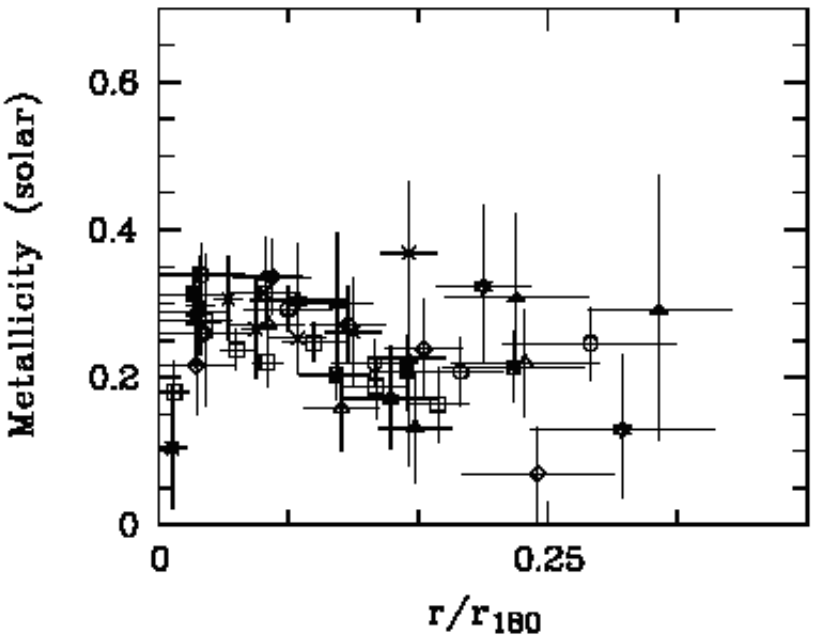

Figure 1.14: Projected abundance profiles clusters without cooling core, Clusters are related to symbols as follows : r180. A119 (lozenges), A754 (crossed squares), A2256 (circles), A2319 (filled triangles), A3266 (open triangles), A3376 (stars), A3627 (crosses), and Coma (squares).(De Grandi & Molendi 2001)

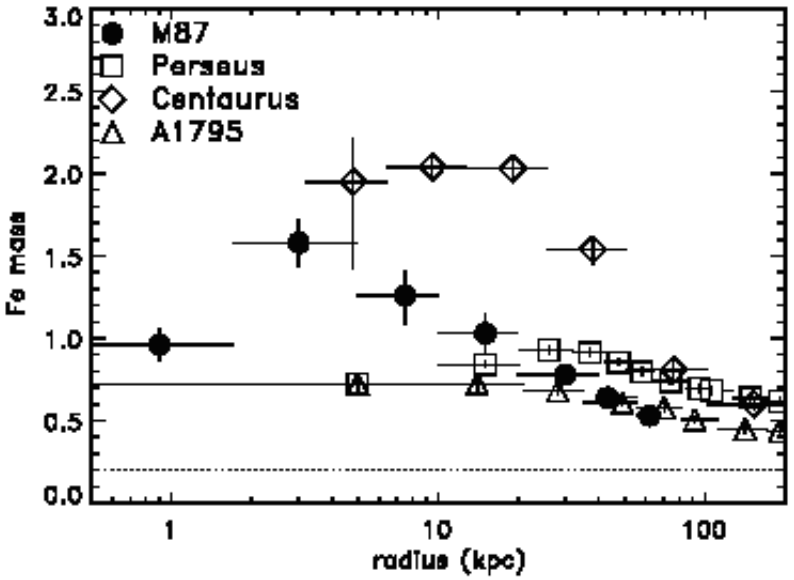

Figure 1.15: The abundance distribution(in unite of solar value) of four clusters: M87/Virgo, Perseus, Centaurus and A1795.(Böhringer et al. 2004)

1.5 The buoyant bubble by AGN jet

Observations have shown that AGN activity has a strong impact on the ICM. Outflows of relativistic plasma from AGNs inflates in the ICM large cavities which are now routinely found in many clusters with cool cores. In Chandra and XMM's images, X-ray cavities have been found to coincide with the radio lobes. So the radio lobes are also called 'radio bubble'(Fig 1.21). Such cavities, filled with relativistic plasma are buoyant and they rise in the gravitational potential of clusters (e.g. Churazov et al. (2001)).

It is also found that a lot of radio lobes are smaller than corresponding x-ray cavities. This is easily explained by the energy loss of relativistic electrons through radio emission, inverse Compton scattering with Cosmic Micro-wave Background(CMB) and coulomb collision with ion. The power of synchrotron radiation is in proportion to square of particle's energy. The radio spectrum index will become steeper and steeper with time. And the radio source will fade in short time$\sim 10^8$years(Heinz et al. 2002). After they fade, the energy loss becomes small(Xiang et al. 2004)(Fig 1.22). Because there exist large amount of relativistic particles with relatively low energy, the cavity will not shrink for long time. They are also called 'ghost bubble'(Clarke et al. 2005).

Another important impact of AGN jet to ICM is that the cool gas in cluster center will be entrained in buoyant bubble. When buoyant bubble lifts, the central cool gas will be transported to large radius in cluster. In the Perseus cluster $H_{I\alpha}$ filaments are found to relate to radio bubble (Fabian et al. 2003) (Fig 1.23). The neutral hydrogen gas emitting $H_{I\alpha}$ usually exists in the center of galaxy. The $H_{I\alpha}$ filaments in Perseus are thought to be the tracer of bubble transportation. Especially, the central cool gas is very high abundance. The cluster's abundance distribution will be changed completely by radio bubble form AGN jet.

1.6 Mergers of clusters and cold fronts

In hierarchical model of cosmic structure evolution, the massive structures are formed by merger of substructures. Merging clusters have indeed been observed (e.g. Fig 1.18). E.g. in Abell 2163, the galaxies clearly form two sub-clusters; the cluster has disturbed X-ray morphology and radio bright regions - typical characteristics of merging clusters (Arnaud et al. 1992, Markevitch & Vikhlinin 2001, Maurogordato et al. 2008).

Hydrodynamic simulations (e.g. Ritchie & Thomas 2002) revealed that the turbulence caused by cluster merging is so big that it can disrupt the cooling flow (cooling core) in cluster. For an equal mass merger (major merger), the cooling cores of both sub-clusters will be disrupted and mixed completely. For the case when a sub-cluster mergers with a much bigger cluster (minor merger), the cooling core of major cluster

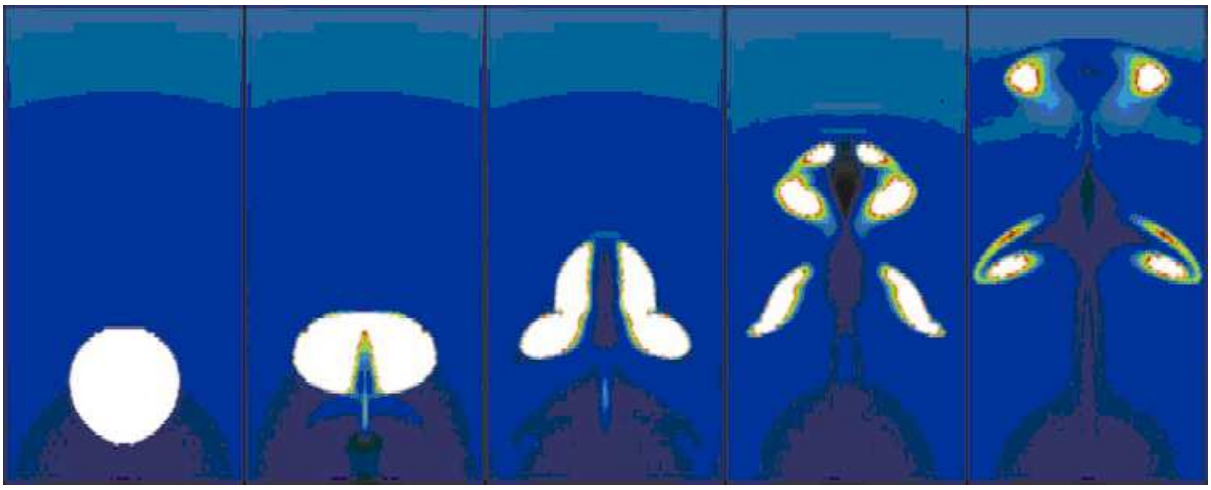

Figure 1.16: The simulation demonstrates that radio-emitting high-energy plasma from AGN jet impacts on the ambient ICM, forms radio bubble and then evolves in ICM. The pictures shows gas temperature map at five stage: 0, 8.4,21,42, and 67Myr in simulation. The box size is $40 \times 20 kpc$. The center of cluster is at the bottom of box.(Churazov et al. 2001)

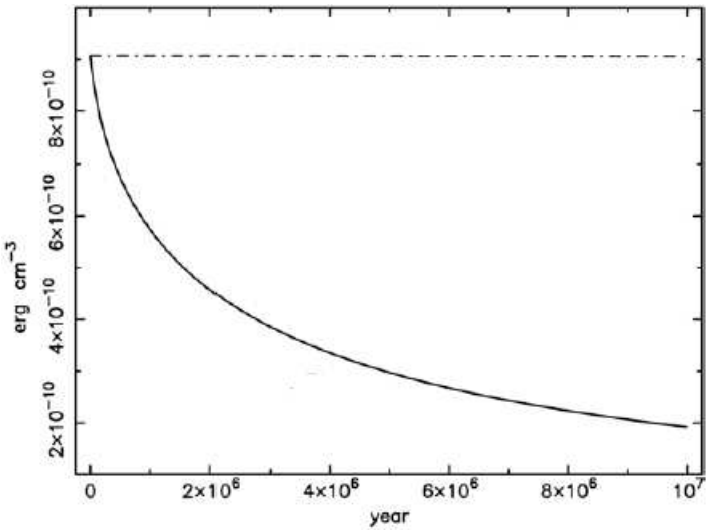

Figure 1.17: The energy density evolution of radio emitting plasma in ICM. The solid line present the energy density of relativistic electrons. The dashed line stands for energy density of relativistic ions. In calculation it is assumed that magnetic field is $50\mu G$, the energy density of CMB is $10^{-14} ergcm^{-3}$, the electron number density of ICM is $0.01 cm^{-3}$ and the radio emitting plasma is mixed with the ICM. For radio emitting plasma, the particles distribute as a power law range from 0.001erg to 5erg. The spectrum index is -2.5. The number density of relativistic electrons is $3.3 \times 10^{-7} cm^{-3}$. And at the beginning, the energy of relativistic ions is the same with that of electrons.(Xiang et al. 2004)

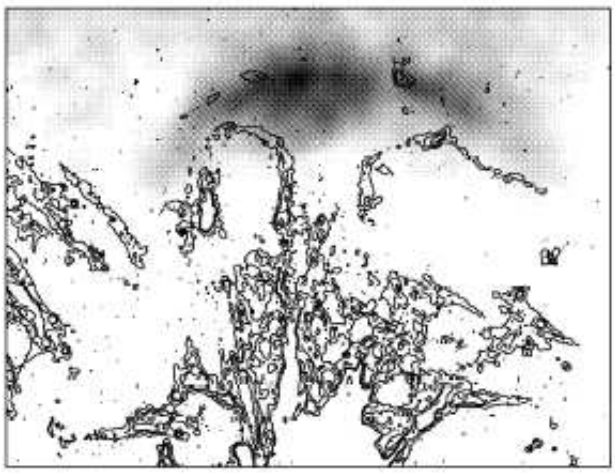

Figure 1.18: The H_α image(contours) of Perseus Cluster center: The image is overlapped with the smoothed x-ray image, which is set to emphasis the rising bubble. The picture shows that the H_α filament is correlated to the trace of bubble moving.(Fabian et al. 2003)

can be destroyed and the cooling core of sub cluster can survive.

In merging, the cool cloud of the sub-cluster will move through the ICM of the main cluster. Its velocity will be comparable to the velocity of cluster galaxies. Such clouds have been observed in merging clusters(e.g. Fig 1.19). They are characterized by a sharp discontinuities in the surface brightness. The gas on bright side is much colder than ambient ICM (e.g. Fig 1.20). The boundary between cold gas and ICM is very sharp and in some case its width is comparable to local mean free path (Vikhlinin et al. 2001). So these clouds are called cold fronts in galaxy clusters.

Cold fronts are also found in clusters without signs of merging (Ghizzardi et al. 2007). So their origins are still under debate. Nevertheless it is believed that differential gas motion is essential feature of most cold fronts. In our work, we perform the simulations that a hot gas flow over a colder gravitationally bound gas cloud with thermal conduction and investigate the impact of thermal conduction and evaporation on interface of cold front.

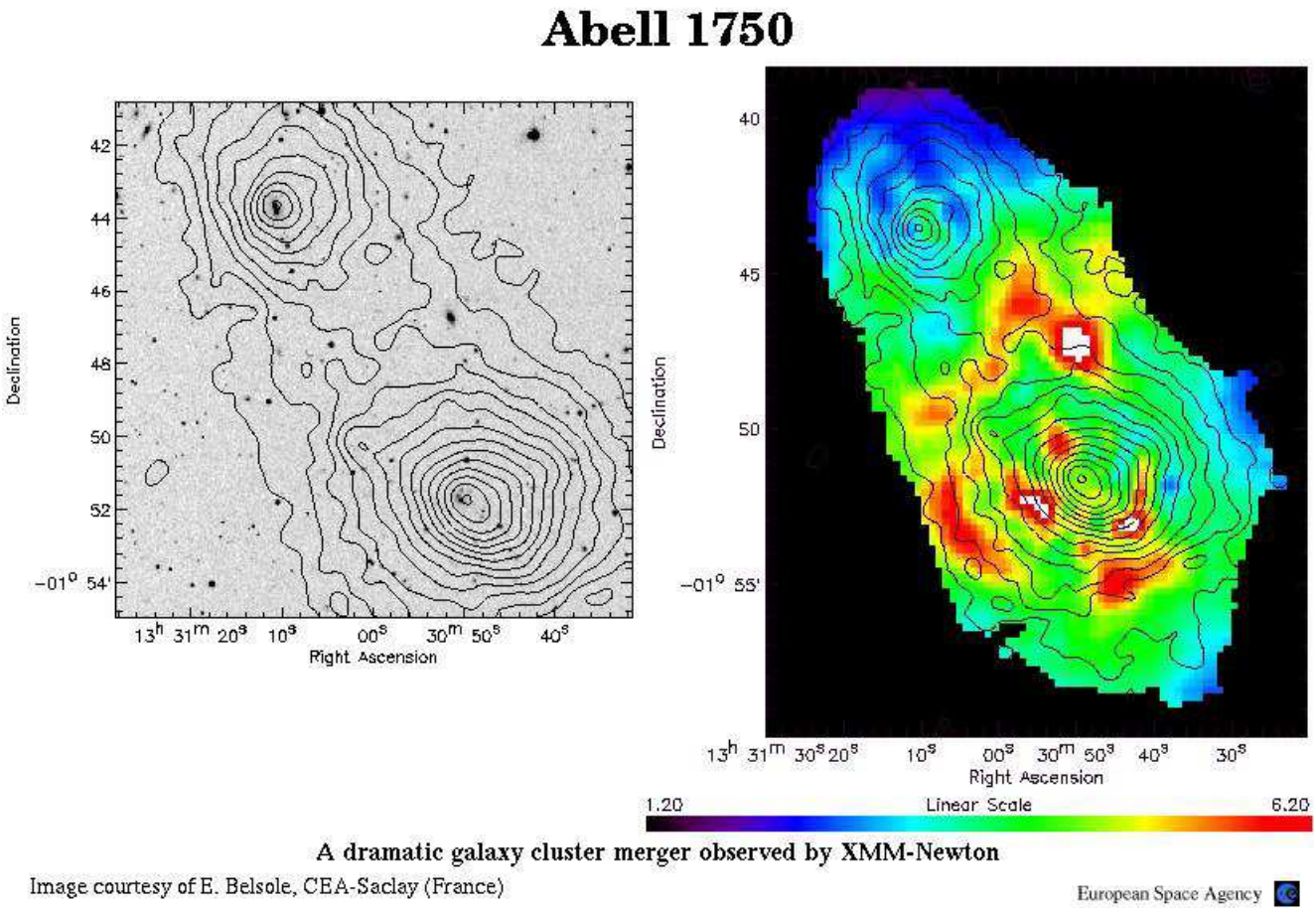

Figure 1.19: The images of merging galaxy cluster Abell 1750: In left panel, the contours of the X-ray brightness (by XMM) are superposed on DSS optical image of the cluster. Two peaks in x-ray apparently lie in north (A1750 N) and south (A1750 C). In right panel, the X-ray brightness contours are plotted over the ICM temperature map by XMM. Blue is cold and red is hot. Irregular hot spots associated with A1750 C. (E. Belsole, CEA-Saclay (France) and ESA.

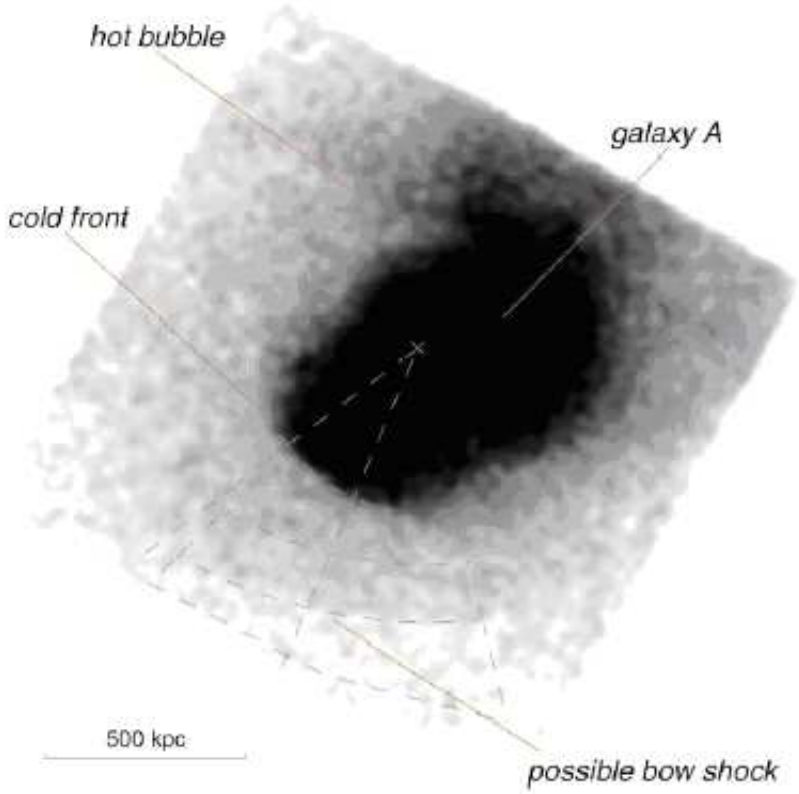

Figure 1.20: The cold front observed in A3667: a 'bullet' moving toward south-west(Vikhlinin et al. 2001).

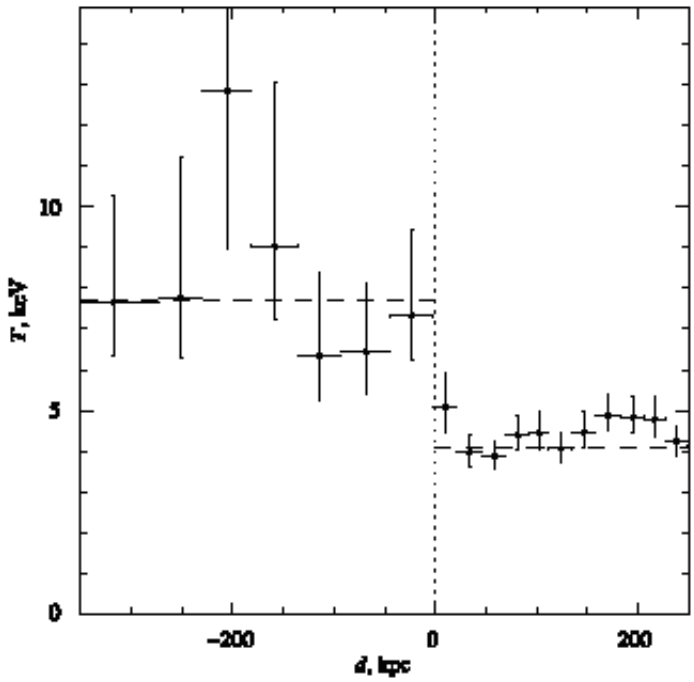

Figure 1.21: The temperature distribution of cold front in A3667(Vikhlinin et al. 2001)).

Bibliography

[1] Abell, G. O. 1958, ApJS, 3, 211

[2] Arnaud, M., Hughes, J. P., Forman, W., Jones, C., Lachieze-Rey, M., Yamashita, K., & Hatsukade, I. 1992, ApJ, 390, 345

[3] Bahcall, N. A. 1977, ARA&A, 15, 505 P. E. J. 2004, ApJ, 607, 800

[4] Böhringer, H., Matsushita, K., Churazov, E., Finoguenov, A., & Ikebe, Y. 2004, A&A, 416, L21

[5] Borgani, S., et al. 2004, MNRAS, 348, 1078

[6] Byram, E. T., Chubb, T. A., & Friedman, H. 1966, Science, 152, 66

[7] Churazov, E., Brüggen, M., Kaiser, C. R., Böhringer, H., & Forman, W. 2001, ApJ, 554, 261

[8] Churazov, E., Forman, W., Jones, C., Böhringer, H. 2003, ApJ, 590, 225

[9] Clarke, T. E., Sarazin, C. L., Blanton, E. L., Neumann, D. M., & Kassim, N. E. 2005, ApJ, 625, 748

[10] David, L. P., Arnaud, K. A., Forman, W., & Jones, C. 1990, ApJ, 356, 32

[11] De Grandi, S., & Molendi, S. 2001, ApJ, 551, 153

[12] den Herder, J. W., et al. 2001, A&A, 365, L7

[13] Ettori, S. 2000, MNRAS, 318, 1041

[14] Faber, S. M., & Gallagher, J. S. 1979, ARA&A, 17, 135

[15] Fabian, A. C. 1994, ARA&A, 32, 277

[16] Fabian, A. C., Celotti, A., Blundell, K. M., Kassim, N. E., & Perley, R. A. 2002, MNRAS, 331, 369

[17] Fabian, A. C., Sanders, J. S., Crawford, C. S., Conselice, C. J., Gallagher, J. S., & Wyse, R. F. G. 2003, MNRAS, 344, L48

[18] Fabricant, D., Lecar, M., & Gorenstein, P. 1980, ApJ, 241, 552

[19] Forman, W., & Jones, C. 1982, ARA&A, 20, 547

[20] Ghizzardi, S., Molendi, S., Rossetti, M., & Leccardi, A. 2007, Heating versus Cooling in Galaxies and Clusters of Galaxies, 33

[21] Govoni, F., Markevitch, M., Vikhlinin, A., VanSpeybroeck, L., Feretti, L., & Giovannini, G. 2004, ApJ, 605, 695

[22] Hanisch, R. J. 1982, A&A, 116, 137

[23] Hashimoto, Y., Barcons, X., Böhringer, H., Fabian, A. C., Hasinger, G., Mainieri, V., & Brunner, H. 2004, A&A, 417, 819

[24] Heinz, S., Choi, Y.-Y., Reynolds, C. S., & Begelman, M. C. 2002, ApJ, 569, L79

[25] Jones, C., & Forman, W. 1984, ApJ, 276, 38

[26] Limber, D. N., & Mathews, W. G. 1960, ApJ, 132, 286

[27] Markevitch, M., Govoni, F., Feretti, L., & Giovannini, G. 2005, X-Ray and Radio Connections (eds. L.O. Sjouwerman and K.K Dyer) Published electronically by NRAO, http://www.aoc.nrao.edu/events/xraydio Held 3-6 February 2004 in Santa Fe, New Mexico, USA, (E8.06) 10 pages,

[28] Markevitch, M., & Vikhlinin, A. 2001, ApJ, 563, 95

[29] Maurogordato, S., et al. 2008, A&A, 481, 593

[30] McHardy, I. M. 1979, MNRAS, 188, 495

[31] McNamara, B. R., et al. 2000, ApJ, 534, L135

[32] Miley, G. 1980, ARA&A, 18, 165

[33] Miley, G. K., Perola, G. C., van der Kruit, P. C., & van der Laan, H. 1972, Nature, 237, 269

[34] Miralda-Escude, J., & Babul, A. 1995, ApJ, 449, 18

[35] Mitchell, R. J., Culhane, J. L., Davison, P. J. N., & Ives, J. C. 1976, MNRAS, 175, 29P

[36] Mitchell, R. J., Dickens, R. J., Burnell, S. J. B., & Culhane, J. L. 1979, MNRAS, 189, 329

[37] Mushotzky, R. F., Serlemitsos, P. J., Boldt, E. A., Holt, S. S., & Smith, B. W. 1978, ApJ, 225, 21

[38] Nevalainen, J., Oosterbroek, T., Bonamente, M., & Colafrancesco, S. 2004, ApJ, 608, 166

[39] Peterson, J. R., Kahn, S. M., Paerels, F. B. S., Kaastra, J. S., Tamura, T., Bleeker, J. A. M., Ferrigno, C., & Jernigan, J. G. 2003, ApJ, 590, 207

[40] Petrosian, V. 2004, 35th COSPAR Scientific Assembly, 35, 4202

[41] Pfrommer, C., & Enßlin, T. A. 2004, MNRAS, 352, 76 Suburbs, 131

[42] Press, W. H., & Schechter, P. 1974, ApJ, 187, 425

[43] Raymond, J. C., Cox, D. P., & Smith, B. W. 1976, ApJ, 204, 290

[44] Rebusco, P., Churazov, E., Böhringer, H., & Forman, W. 2005, MNRAS, 359, 1041

[45] Rebusco, P., Churazov, E., Böhringer, H., & Forman, W. 2006, MNRAS, 372, 1840

[46] Ritchie, B. W., & Thomas, P. A. 2002, MNRAS, 329, 675

[47] Sanders, J. S., Fabian, A. C., Allen, S. W., & Schmidt, R. W. 2004, MNRAS, 349, 952

[48] Sarazin, C. L., & Bahcall, J. N. 1977, ApJS, 34, 451

[49] Simionescu, A., Werner, N., Finoguenov, A., Böhringer, H., & Brüggen, M. 2008, A&A, 482, 97

[50] Springel, V., et al. 2005, Nature, 435, 629

[51] Springel, V. 2005, MNRAS, 364, 1105

[52] Strüder, L., et al. 2001, A&A, 365, L18

[53] Turner, M. J. L., et al. 2001, A&A, 365, L27

[54] Vikhlinin, A., Markevitch, M., & Murray, S. S. 2001, ApJ, 551, 160

[55] Wolf, M. 1906, Astronomische Nachrichten, 170, 211

[56] Wu, X.-P., & Fang, L.-Z. 1997, ApJ, 483, 62

[57] Xiang, F., Chen, Y., Wu, M., Lu, F.-J., Song, L.-M., & Jia, S.-M. 2004, Chinese Astronomy and Astrophysics, 28, 387

[58] http://www.chandra.harvard.edu

[59] http://xmm.esac.esa.int

2 On the width of cold fronts in clusters of galaxies due to conduction

Mon.Not.R.Astron.Soc., 2007, 379, 1325

F. Xiang, E. Churazov, K. Dolag, V. Springel, A. Vikhlinin

Abstract

We consider the impact of thermal conduction in clusters of galaxies on the un-magnetized interface between a cold gaseous cloud and a hotter gas flowing over the cloud (the so-called cold front). We argue that near the stagnation point of the flow conduction creates a spatially extended layer of constant thickness Δ, where Δ is of order $\sim \sqrt{kR/U}$, and R is the curvature radius of the cloud, U is the velocity of the flow at infinity, and k is the conductivity of the gas. For typical parameters of the observed fronts, one finds $\Delta \ll R$. The formation time of such a layer is $\sim R/U$. Once the layer is formed, its thickness only slowly varies with time and the quasi-steady layer may persist for many characteristic time scales. Based on these simple arguments one can use the observed width of the cold fronts in galaxy clusters to constrain the effective thermal conductivity of the intra-cluster medium.

2.1 Introduction

Chandra observations of galaxy clusters often show sharp discontinuities in the surface brightness of the hot intra-cluster medium (ICM) emission (Markevitch et al., 2000, Vikhlinin, Markevitch, Murray, 2001, see Markevitch & Vikhlinin 2007 for a review). Most of these structures have lower temperature gas on the brighter (higher density) side of the discontinuity, contrary to the expectation for non-radiative shocks in the ICM. Within the measurement uncertainties, the pressure is continuous across these structures, suggesting that they are contact discontinuities rather than shocks. In the literature these structures are now called "cold fronts".

There are several plausible mechanisms responsible for the formation of such cold fronts, all of them involving relative motion of the cold and hot gases. Below we will consider the case of a hot gas flow over a colder gravitationally bound gas cloud, which is a prototypical model of a cold front. In such a situation one expects that ram pressure of the hotter gas strips the outer layers of the colder cloud, exposing denser gas layers and forming a cold front near the stagnation point of the hot flow (Markevitch et al., 2000, Vikhlinin et al., 2001a, Bialek, Evrard and Mohr, 2002, Nagai & Kravtsov, 2003, Acreman et al., 2003, Heinz et al., 2003, Asai, Fukuda & Matsumoto, 2004, 2007, Mathis et al., 2005, Tittley & Henriksen, 2005, Takizawa, 2005, Ascasibar & Markevitch 2006) .

Some of the observed cold fronts are remarkably thin. For example, the width of the front in Abell 3667 (Vikhlinin et al., 2001a) is less than 5 kpc, which is comparable to the electron mean free path. Given that the temperature changes across the front by a factor of ~ 2, thermal conduction (if not suppressed) should strongly affect the structure of the front (e.g. Ettori & Fabian, 2000). In fact, suppression of conduction by magnetic fields is likely to happen along the cold front since gas motions on both sides of the interface may produce preferentially tangential magnetic field, effectively shutting down the heat flux across the front (e.g. Vikhlinin et al., 2001b, Narayan & Medvedev, 2001, Asai et al., 2004, 2005, 2007, Lyutikov 2006). While magnetic fields are hence likely to play an important role in shaping cold fronts, it is still interesting to consider the expected structure of a cold front in the idealized case of an unmagnetized plasma.

The structure of this paper is as follows. In Section 2, basic equations are listed and a toy model of a thermally broadened interface between cool and hot gas is discussed. In Section 3, we present the results of numerical simulations of hot gas flowing past a cooler gas cloud. In Section 4, we discuss how limits on the effective conductivity can be obtained for the observed cold fronts. Finally, we summarize our findings in Section 5.

2.2 Thermal conduction near the stagnation point of the flow

2.2.1 Basic equations

We parameterize the isotropic thermal conductivity k as

$$k = f \times k_0, \tag{2.1}$$

where $f < 1$ is the suppression coefficient of the conductivity relative to the conductivity k_0 of an unmagnetized plasma (Spitzer 1962, Braginskii 1965):

$$k_0 = 4.6 \times 10^{13} \left(\frac{T}{10^8\,\mathrm{K}}\right)^{5/2} \left(\frac{\ln\Lambda}{40}\right)^{-1} \mathrm{erg\ cm^{-1}\ s^{-1}\ K^{-1}}, \tag{2.2}$$

where T is the gas temperature, and $\ln\Lambda$ is the Coulomb logarithm.

If the scale length of temperature gradients is much larger than the particle mean free path, then saturation of the heat flux (Cowie & McKee, 1977) can be neglected and the evolution of the temperature distribution can be obtained by solving the mass, momentum and energy conservation equations with the heat diffusion term $\nabla \cdot \mathbf{k}\nabla\mathbf{T}$ in the energy equation (e.g. Landau & Lifshitz, 1959):

$$\frac{\partial \rho}{\partial t} + \nabla \cdot (\rho \mathbf{v}) = \mathbf{0}, \tag{2.3}$$

$$\frac{\partial \mathbf{v}}{\partial t} + (\mathbf{v} \cdot \nabla)\,\mathbf{v} = -\frac{1}{\rho}\nabla \mathbf{p} + \mathbf{g}, \tag{2.4}$$

$$\frac{\partial}{\partial t}\left(\frac{\rho \mathbf{v}^2}{2} + \rho\epsilon\right) = \nabla \cdot \mathbf{k}\nabla\mathbf{T} - \nabla \cdot \rho \mathrm{v}\left(\frac{\mathbf{v^2}}{\mathbf{2}} + \omega\right), \tag{2.5}$$

where ρ is the gas density, p is the gas pressure, g is the gravitational acceleration, and v is the gas velocity. We adopt an ideal gas with $\gamma = 5/3$, where $\epsilon = \frac{1}{\gamma-1}\frac{k_B T}{\mu m_p}$, $\omega = \frac{\gamma}{\gamma-1}\frac{k_B T}{\mu m_p}$, and $p = \frac{\rho}{\mu m_p} k_B T$.

In the next section we first consider the simplified case of passive scalar diffusion in a time independent velocity flow, while in Section 2.3 we discuss numerical solutions of the above equations.

2.2.2 Toy model

Churazov & Inogamov (2004) noted that the behaviour of a conducting layer in cold fronts should be similar to the behaviour of a viscous layer near a plate or near the surface of a blunt body (see e.g. Batchelor, 1967). When the fluid is advected along the surface, the thickness of the layer grows in proportion to the square root of the advection time. Near the stagnation point, the velocity of the flow

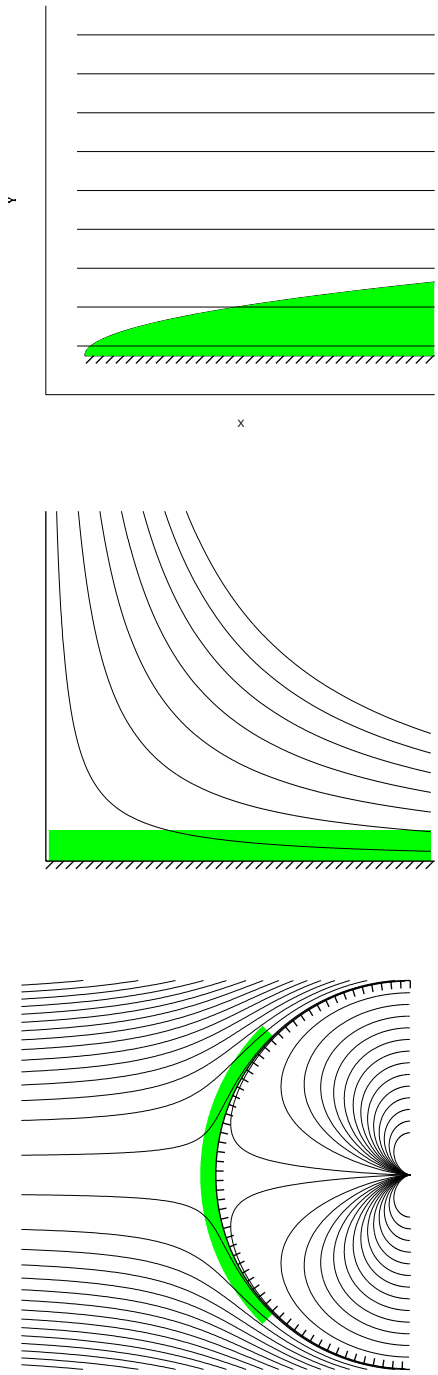

Figure 2.1: Examples of simple potential flows: uniform flow past a plate (left), flow into a 90 degree corner (middle) and flow past a sphere (right). Streamlines are shown as thin solid lines. The shaded areas schematically indicate the width of the layer formed by diffusion.

increases linearly with the distance from the stagnation point and the characteristic advection time is approximately constant. Therefore the thickness of the layer can also be approximately constant. Below we provide a more rigorous justification of this picture.

Let us consider the simple case of diffusion of a passive scalar ψ in a potential flow of an incompressible fluid. The diffusion coefficient D is assumed to be constant[1] and the velocity field is known and constant with time. The diffusion equation

$$\frac{\partial \psi}{\partial t} + \nabla \cdot (\mathbf{v}\psi) - \mathbf{D}\boldsymbol{\Delta}\psi = \mathbf{0} \tag{2.6}$$

is supplemented by static boundary conditions at the surface of the body and at large distance from the body. For a steady state solution ($\frac{\partial \psi}{\partial t} = 0$) and for an incompressible fluid ($\nabla \cdot \mathbf{v} = \mathbf{0}$) the above equation reduces to

$$\mathbf{v} \cdot \nabla\psi - \mathbf{D}\boldsymbol{\Delta}\psi = \mathbf{0}. \tag{2.7}$$

In the simplest case of a uniform flow along the "heated" plate (Fig. 2.1 left), $v_x = u = \text{const}$ and $v_y = 0$. At sufficiently large distance from the leading edge of the plate, the derivative $\frac{\partial^2 \psi}{\partial^2 x}$ can be neglected and equation (2.7) can be written as

$$u\frac{\partial \psi}{\partial x} - D\frac{\partial^2 \psi}{\partial y^2} = 0. \tag{2.8}$$

An obvious solution in the form $\psi = f(y/\sqrt{x})$ is given by

$$\psi = (\psi_1 - \psi_2)\ \mathrm{Erf}\left(\sqrt{\frac{u}{2Dx}}y\right) + \psi_2, \tag{2.9}$$

where ψ_2 and ψ_1 are the values of the scalar at the plate and at infinity, respectively. The width of the interface is therefore $\Delta y = \sqrt{\frac{2D}{u}x}$ and it increases with the distance x from the leading edge of the plate as $\sqrt{x}$. Since it takes a time $t = x/u$ for the gas to flow from the edge of the plate to a given position x, the width of the diffusive layer is simply $\sim \sqrt{Dt} = \sqrt{Dx/u}$.

Consider now a potential flow into a 90 degrees corner (Fig. 2.1 middle), governed by the velocity potential $\phi = Ar^2 \cos 2\theta$ (see e.g. Lamb 1932, for various examples of potential flows). Here r is the distance from the corner and θ is angle from the horizontal axis. In this case the velocity components are $v_x = 2Ax$ and $v_y = -2Ay$. An obvious solution to equation (2.7) is then

$$\psi = (\psi_1 - \psi_2)\ \mathrm{Erf}\left(\sqrt{\frac{A}{D}}y\right) + \psi_2, \tag{2.10}$$

[1] We use the notation D in this section for constant diffusion coefficient to distinguish it from the temperature dependent heat conductivity k.

with the width $y = \sqrt{\frac{D}{A}}$ of the interface being independent of x. The reason for this behaviour is clear: the acceleration of the (incompressible) fluid along the interface causes a contraction of the fluid elements perpendicular to the direction of the acceleration. While diffusion is trying to make the interface broader, the motion of the fluid towards the interface compensates for the broadening of the interface, and a steady state is reached (Fig. 2.1 middle).

The potential flow past a cylinder or sphere behaves qualitatively similar (Fig. 2.1 right). Indeed, in the vicinity of the stagnation point (for $\theta \ll 1$), the radial and tangential components can be written as (flow is from the right to the left, angle is counted clockwise from the $-x$ direction):

$$\begin{aligned} v_r &= -U\left(1 - \frac{R^2}{r^2}\right)\cos\theta \approx -2U\frac{\eta}{R} \\ v_\theta &= U\left(1 + \frac{R^2}{r^2}\right)\sin\theta \approx 2U\frac{\zeta}{R}, \end{aligned} \tag{2.11}$$

for a cylinder and

$$\begin{aligned} v_r &= -U\left(1 - \frac{R^3}{r^3}\right)\cos\theta \approx -3U\frac{\eta}{R} \\ v_\theta &= U\left(1 + \frac{R^3}{2r^3}\right)\sin\theta \approx \frac{3}{2}U\frac{\zeta}{R} \end{aligned} \tag{2.12}$$

for a sphere. Here U is the velocity at infinity, R is the radius of the cylinder or sphere, $\eta = r - R$ and $\zeta = R\sin\theta$.

In the same approximation as for the cases discussed above (where the spatial derivative of ψ along ζ is neglected) the diffusion equation reduces to

$$-v_r\frac{\partial\psi}{\partial r} - D\frac{\partial^2\psi}{\partial r^2} = 0, \tag{2.13}$$

and the width of the interface over the radius is set by the diffusion coefficient D and the coefficient C in the relation $v_r = -C\eta$, yielding

$$\Delta r \approx \sqrt{\frac{2D}{C}} = \begin{cases} \sqrt{D\frac{R}{U}} & \text{cylinder} \\ \sqrt{\frac{2}{3}D\frac{R}{U}} & \text{sphere.} \end{cases} \tag{2.14}$$

In this case the width of the interface is also constant along the surface of the cylinder or sphere (Fig. 2.1 right).

One can also consider a closer analogue of a flow past a spherical cloud by extending the solution for a potential flow into the inner part of the cylinder or sphere, as

illustrated in Fig. 2.1. In this model there is a circulation flow of gas inside the cloud, and the tangential component of the velocity is continuous across the boundary while the normal component is zero at the boundary. We can further allow for different densities ρ_1 and ρ_2 outside and inside of the boundary if all velocities inside are scaled by a factor $\sqrt{\rho_1/\rho_2}$. The resulting configuration can be considered as an idealized (and unstable) analogue of a hot flow past a colder cloud in the absence of gravity (see also Heinz et al., 2003). Allowing different diffusion coefficients D_1 and D_2 in the flow outside and inside the boundary, and requiring the solution ψ and its spatial derivative to be continuous across the interface, yields the following solution in the vicinity of the stagnation point:

$$\begin{aligned}
\psi &= (\psi_1 - \psi_m)\ \mathrm{Erf}\left(\sqrt{\frac{C_1}{2D_1}}(r - r_0)\right) + \psi_m \quad \text{outside,} \\
\psi &= (\psi_m - \psi_2)\ \mathrm{Erf}\left(\sqrt{\frac{C_2}{2D_2}}(r - r_0)\right) + \psi_m, \quad \text{inside} \\
\psi_m &= \frac{\psi_1 + \psi_2 \frac{D_2}{D_1}\frac{C_1}{C_2}}{1 + \frac{D_2}{D_1}\frac{C_1}{C_2}}.
\end{aligned}$$

Here r_0 is the radius of the boundary, ψ_1 and ψ_2 are the values far from the interface, $C_2 = C_1\sqrt{\rho_1/\rho_2}$, and $C_1 = 2U/R$ for a cylinder or $C_1 = 3U/R$ for a sphere, respectively. The width of the interface is again constant along the boundary.

The same answer is obviously valid for any idealized flow of this type: near the stagnation point the width of the "heated" layer does not change along the surface of the body. Real cold fronts are of course much more complicated structures. However, the acceleration of the flow along the interface and the simultaneous contraction in the perpendicular direction are generically present also here. It can therefore be expected that the width of the interface will be similarly constant in real cold fronts. A simple extension of the above toy model can be obtained by allowing for gas compressibility and a temperature dependent conductivity, i.e. by considering the full system of equations (2.3)-(2.5) with conductivity according to eq. (2.2). An expansion of heated layers and simultaneous contraction of cooled layers on the other side of the interface will certainly modify the flow, but for the transonic flows of interest here we might expect that the results obtained for a toy model will still be approximately valid. In the next section we verify this prediction using numerical simulations.

2.3 Numerical simulations

For our numerical experiments, we used the TreeSPH code GADGET-2 (Springel, 2005) combined with the implementation of thermal conduction discussed by Jubelgas, Springel & Dolag (2004), which accounts both for the saturated and unsaturated regimes of the heat flux.

The simulations were intended to illustrate a simple toy model, described in section 2.2.2, rather than to provide a realistic description of the observed cold fronts. The specific goal was to see the impact of the flow stretching near the stagnation point on the width of the interface set by conduction. With this in mind we intentionally restricted ourselves to a 2D geometry and an unmagnetized plasma. For a 3D calculation of magnetized clouds see Asai et al. (2007). The self gravity of gas particles was also neglected in our idealized simulations and all gas motions were happening in a static gravitational potential. Given that the typical gas mass fraction in clusters is of order 10-15 per cent, the self gravity of gas particles is likely to be a second order effect. A more significant simplification is the assumption of a static potential, since at least some of the cold fronts are caused by cluster mergers where strong changes of the potential are possible. Formation of cold fronts in the appropriate cosmological conditions was considered by e.g. Bialek et al. (2002), Nagai & Kravtsov (2003), Mathis et al. (2005), see also Tittley & Henriksen (2005) and Ascasibar & Markevitch (2006). Our illustrative 2D simulations, described below, can be viewed as a "minimal" configuration which allows us to see the effect of flow stretching and to extend the toy model to the case of a compressible gas and a temperature dependent diffusion coefficient.

2.3.1 Initial conditions

Our 2D simulations of cold fronts in clusters were carried out in a 8x4 Mpc periodic box. We represented the cluster with a static King gravitational potential of the form

$$\phi = -9\sigma^2 \frac{\ln\left[x + \sqrt{1+x^2}\right]}{x}, \tag{2.15}$$

with $\sigma = 810\,\mathrm{km\,s^{-1}}$, $x = r/r_c$ and $r_c = 300$ kpc. The initial temperature and density distributions were set to

$$(T_e, \rho) = \begin{cases} (T_1, \frac{\rho_1}{(1+x^2)^{\frac{3}{2}}}) & x < x_{\rm out} \\ (T_2, \frac{\rho_2}{(1+x^2)^{\frac{3}{2}\frac{T_1}{T_2}}}) & x > x_{\rm out} \end{cases} \tag{2.16}$$

where

$$\rho_2 = \frac{\rho_1}{(1+x_{\rm out}^2)^{\frac{3}{2}}} \frac{T_1}{T_2} \left[(1+x_{\rm out}^2)^{\frac{3}{2}} \frac{T_1}{T_2} \right], \tag{2.17}$$

and $kT_1 = \mu m_p \sigma^2 \approx 4$ keV. Thus the temperature and density make a jump at $x_{\rm out}$, while the pressure is continuous. In our runs, $T_2 = 8$ keV, $x_{\rm out} = 1$, $\mu = 0.61$, and $\rho_1 = 6.6 \times 10^{-26}$ g cm^{-3}. The gas velocity was set to zero for $x < x_{\rm out}$ and to $u = 2000$ km s^{-1} for $x > x_{\rm out}$. The corresponding Mach number relative to the hot 8 keV gas is $\sim$1.3 (neglecting further acceleration of the flow in the cluster potential).

10^6 gas particles of equal mass were distributed over the computational volume as a Poissonian sample of the initial density distribution described above. The gas temperature for each particle was set to T_1 or T_2 depending on the position of the particle. The Poissonian noise introduced by this procedure leads to small-scale (and small amplitude) pressure/entropy perturbations in the initial conditions. Shortly after the beginning of the simulations, the over-dense regions expand and create a pattern of ripples in the temperature distribution (see Fig. 2.2, top panel). We stress that the presence of these ripples is a direct consequence of the choice of initial particle positions and it does not mean that the number of particles is insufficient to properly resolve the cold front. A comparison of three runs with 3 10^5, 10^6 and 3 10^6 particles with the same initial condictions and the conduction suppression coefficient $f = 0.01$ yielded practically undistinguishable results in terms of the cold front structure. As these ripples do not affect the overall structure of the flow no attempt was made to correct the initial conditions for this effect. These ripples are also a useful visual indicator of the impact of thermal conduction on the small-scale temperature structures in the flow (see Fig. 2.2).

Our choice of initial conditions has been motivated by the cold front in the cluster Abell 3667 (Vikhlinin et al., 2001), but we did not try to accurately reproduce all the observed properties of this cluster. In particular, the location and the strength of the shock in our model need not be the same as in A3667. Nevertheless, the most important feature of A3667 – a cool gas cloud inside a hotter and less dense flow – is present in our simulations, allowing us to study the impact of thermal conduction on the interface between the cloud and the flow. To this end we carried out four runs where the coefficient of the thermal conduction efficiency was set to $f = 0$, 0.01, 0.1, and 0.5, respectively.

2.3.2 Results

In Fig. 2.2, we show the temperature distributions for all four runs 1.3 Gyr after the start of the simulations. Immediately after the beginning of the simulations a shock starts to propagate upstream through the hot flow, forming a clearly visible bow shock. Because of the acceleration in the cluster potential, the Mach number of the shock is $\sim$1.7 (rather than 1.3) and the temperature behind the shock is also rather high (10-15 keV).

The cool cloud is first pushed back by the ram pressure of the gas and then (slowly) oscillates near an equilibrium position. At 1.3 Gyr, there are still some residual motions clearly associated with the specific initial conditions, but these motions are quite gradual. This can also be seen in the gas velocity field, which is plotted in Fig. 2.3. It shows a clearly visible velocity jump at the shock front, and inside and around the cloud, circular motions are present, broadly resembling the velocity field shown in Fig. 2.1. Such circular motions inside the cloud lead to a transport of low entropy gas from the centre of the cloud towards the stagnation point (Heinz et al.,

2003). As a result of adiabatic expansion of the transported gas its temperature drops to ~ 3 keV, below the initial value of 4 keV.

Since after 1.3 Gyrs much of the relaxation from the initial state already took place, we compare the runs with different conductivity at this time. The effect of increasing the efficiency of thermal conduction is clearly visible in the snapshots shown in Fig. 2.2. First of all, small scale temperature variations present in the initial conditions are smoothed out in all runs where thermal conduction is present. Secondly, with the increase of f the interface separating the cloud and the hot flow becomes less and less sharp. This is seen more explicitly in the temperature profiles across the interface (along the symmetry axis of the cloud), which are shown in Fig. 2.4. In this figure (and in the subsequent figures), the distance (plotted along the abscissa axis) is measured from the approximate centre of the cloud. Since the cloud is not perfectly spherical, its position varies slowly with time. As its centre is hence not accurately known, all profiles shown in Fig. 2.4 were shifted along the abscissa axis to have the temperature value 6 keV gas at the same position.

The sharpest profile corresponds of course to the run without conduction, and in this case some small-scale fluctuations left over from the initial conditions can still be seen in the profile. This run also sets a useful benchmark for comparison with the other simulations, for example, it indicates the numerical resolution available for representing the interface. We see that for values of f larger than 0.01 the impact of thermal conduction on the width of the interface can be well resolved with our numerical setup. For runs with $f = 0.01$, 0.1 and 0.5, the small-scale fluctuations in the temperature distribution are absent and the effective thickness of the interface gradually increases.

We can now verify our simple predictions based on the toy model of diffusion of a passive scalar in a potential flow. We first consider our finding that after an initial settling time of order R/U the interface evolves to a quasi-steady state. This is indeed seen in Fig. 2.6, where the temperature profiles along the symmetry axis are shown for $t = 0.2$, 0.4, 0.8, and 1.3 Gyr since the beginning of the simulations. While there is clear evolution of the profile (e.g. in terms of the maximal or minimal temperatures) the shape of the interface is very similar at all times.

Another expectation is that the thickness of the interface is the same along the interface (as long as the distance from the stagnation point is much less the the cloud curvature radius). Indeed, the profiles measured at different distances from the stagnation point (Fig. 2.7) look very similar. In this figure, the profiles were calculated along directions making different angle with respect to the symmetry axis of the cloud (red lines in Fig. 2.2). This means that when deriving an effective conduction coefficient from the observed cold fronts one can use the profile averaged over a large part of the interface, rather than being constrained to small sectors of the front.

Thus the results of the numerical simulations are broadly consistent with the expectations derived earlier: once the front is formed, it has a width constant in time

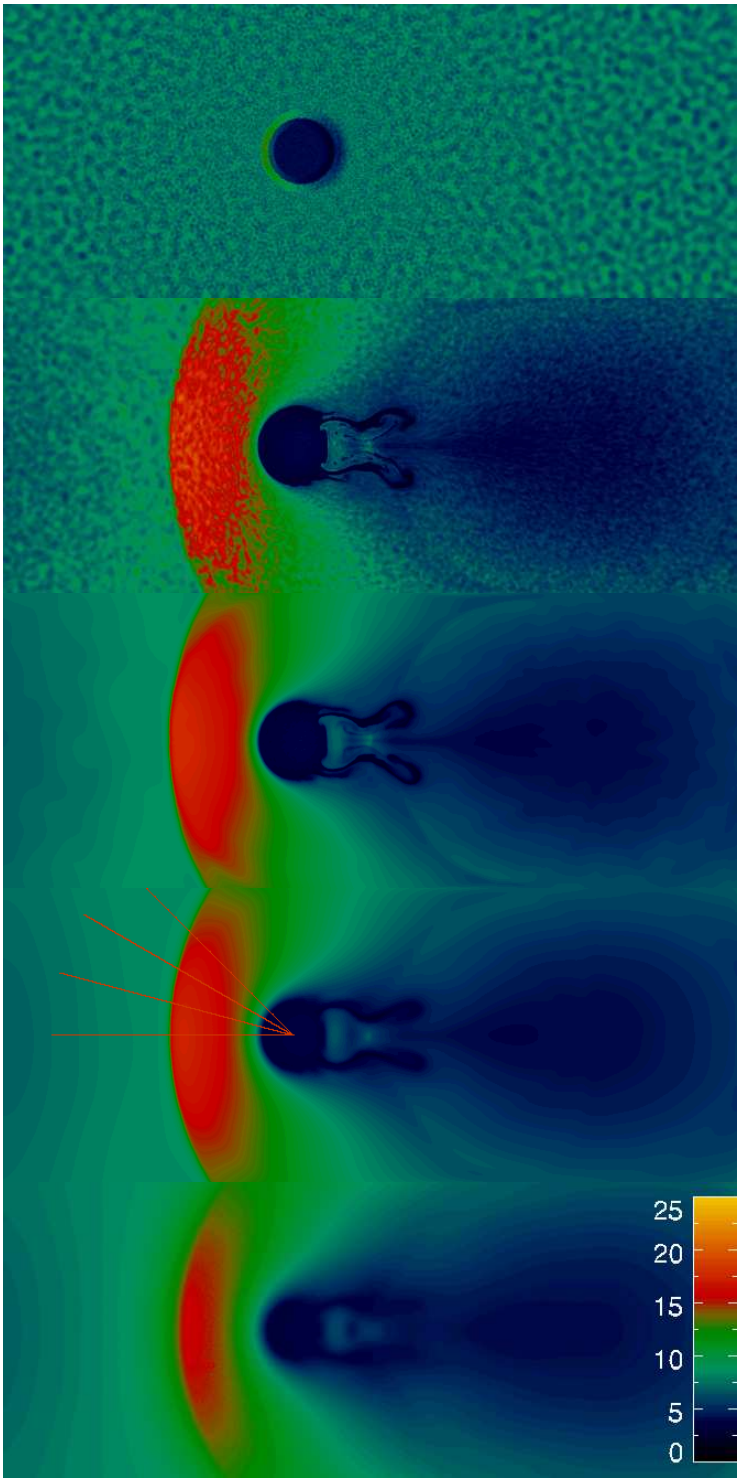

Figure 2.2: Snapshots of the temperature distribution for a 2D flow of hot (8 keV) gas past a cold (4 keV) cloud. The image sizes are 6.7 by 2.7 Mpc. The top panel corresponds to a moment shortly after the start of the simulations. In the other panels, the temperature distributions at $t = 1.3$ Gyr after the beginning of the simulations are shown as a function of the strength of thermal conduction. The conduction suppression coefficient for these panels is $f = 0$, 0.01, 0.1, and 0.5, respectively. Thus the second panel shows the run without conduction, while the bottom panel corresponds to a conductivity equal to half the Spitzer-Braginskii value. The temperature structure of the interface plotted in subsequent figures was measured along the red lines shown in one of the panels.

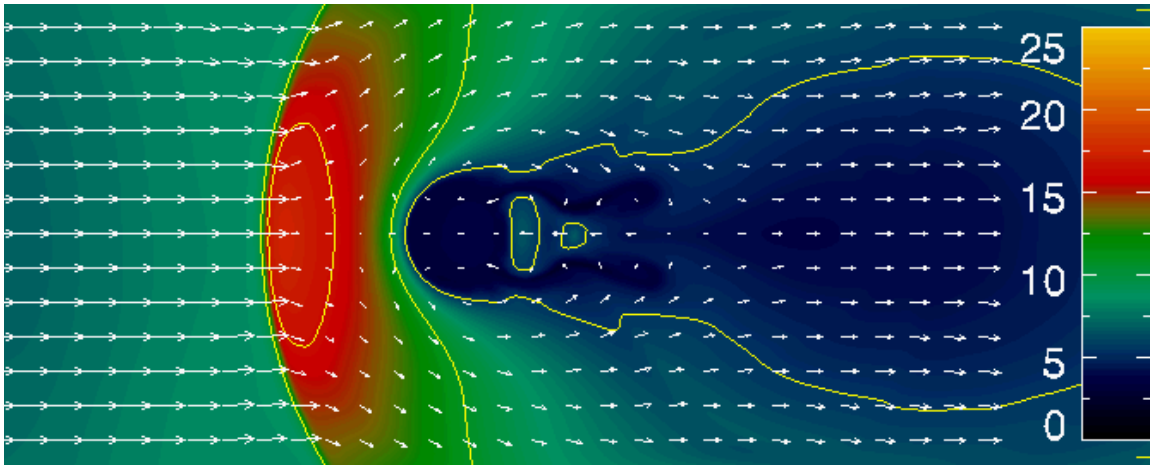

Figure 2.3: Snapshot of the temperature distribution at $t = 1.3\,\mathrm{Gyr}$ after the start of a simulation with conductivity coefficient $f = 0.1$, with the velocity field superposed.

and constant along the interface.

2.4 Simple estimates of the interface width

We are now looking for a simple 1D problem for a compressible fluid which has a solution that can provide a qualitative approximation of the cold front structure. The analogy with the problems considered in Section 2.2.2 suggests that the width of the interface should scale as $\sqrt{Dt_s}$, where D is the effective diffusion coefficient (thermal conductivity) and t_s is the effective time scale. For the flows in Section 2.2.2, a reasonable choice was $t_s \sim R/U$, where R is the curvature radius of the interface and U is the velocity of the flow at infinity. Of course, this result was derived for a potential flow, and for more realistic cases it might be more correct to recast t_s in the form $t_s = \left(\frac{\mathrm{d}v_r}{\mathrm{d}r}\right)^{-1}$, where v_r is the velocity component perpendicular to the interface. Indeed, from Eqs. (2.13) and (2.14) it is clear that that this quantity (i.e. the gradient of the radial velocity component) enters the expression of the interface width. We can hence try to obtain an approximate solution for the front structure by considering a 1D time dependent diffusion equation[2], starting from a Heaviside step function for the initial temperature distribution and taking the solution at time t_s. The hope is that for this choice of t_s the most basic properties of the interface structure will be captured.

We also assume that all velocities in the vicinity of the interface are small compared to the sound speed, all quadratic terms in v can be neglected and that the pressure is

[2] An alternative approach is to incorporate the velocity field of the base flow into the energy conservation equation and to look for a steady state solution.

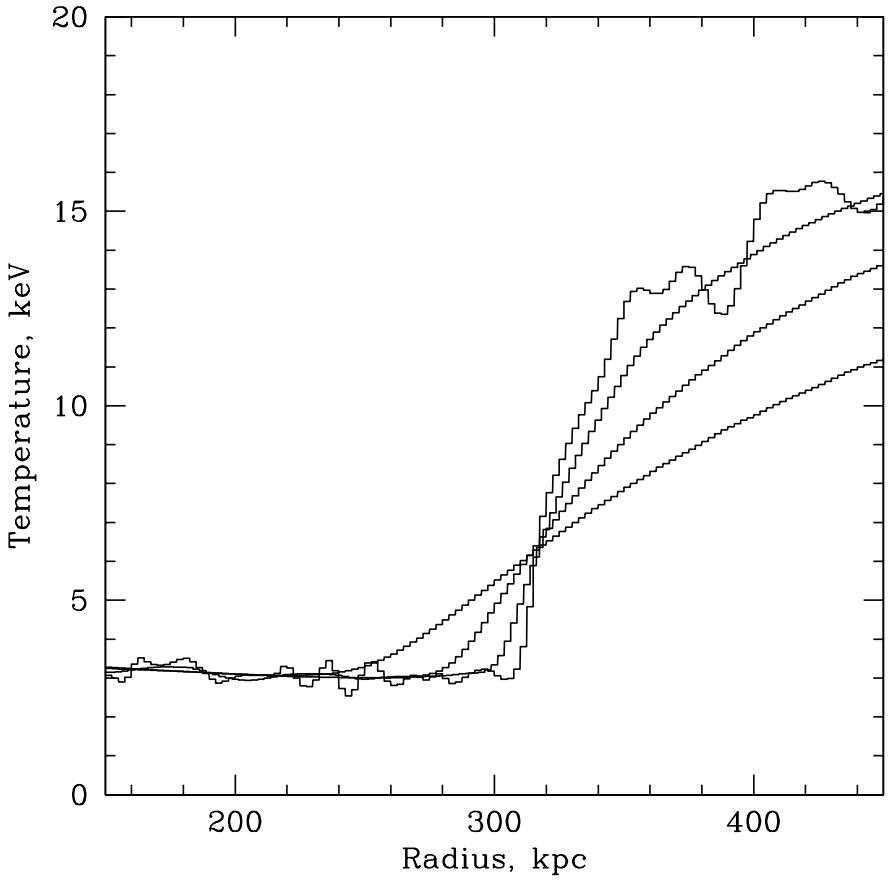

Figure 2.4: Temperature profiles along the symmetry axis of the cloud at $t = 1.3$ Gyr after the start of the simulations, for different conduction suppression coefficients equal to $f = 0$, 0.01, 0.1, and 0.5. The distance is measured from the centre of the cold cloud.

approximately constant across the interface. Then the gas density is $\rho = \rho_0 \frac{T_0}{T}$, where $\rho_0 T_0 = P_0$ is fixed by the initial pressure. In this approximation, the heat diffusion equation reduces to

$$\frac{\partial T}{\partial t} = \lambda \frac{\partial}{\partial x} k \frac{\partial T}{\partial x} - \lambda \frac{k}{T} \left(\frac{\partial T}{\partial x} \right)^2 , \tag{2.18}$$

where $\lambda = \frac{\gamma - 1}{\gamma} \frac{\mu m_p}{\rho k_B}$. This equation is very similar to the standard diffusion equation in solids, except for the second term in the r.h.s. which accounts for gradual expansion of the heated gas, and for the contraction of the cooled gas in order to maintain constant pressure across the interface.

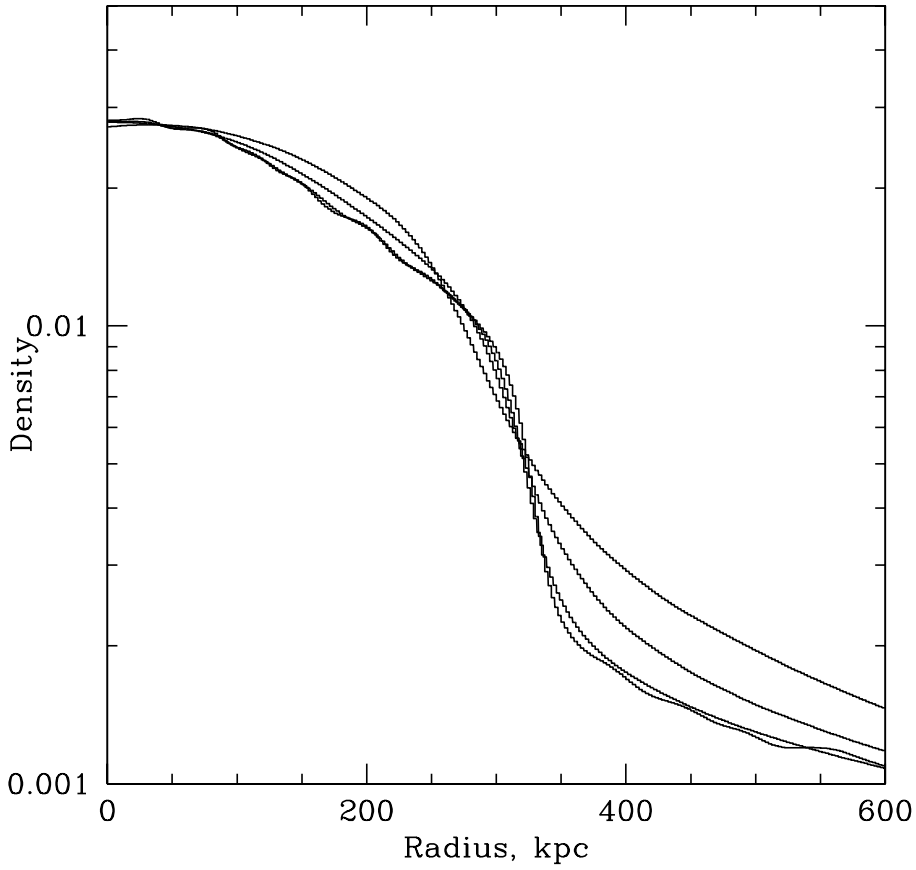

Figure 2.5: Gas density profiles along the symmetry axis of the cloud at $t = 1.3\,\mathrm{Gyr}$ after the start of the simulations, for different conduction suppression coefficients equal to $f = 0$, 0.01, 0.1, and 0.5. The distance is measured from the centre of the cold cloud.

Equation (2.18) can be readily integrated. We set the initial values of the temperature to 3 and 15 keV on the two sides of the interface, respectively, and the electron density to $10^{-2}\,\mathrm{cm}^{-3}$ on the cool side to approximately reproduce the properties of the simulated front, as shown in Fig. 2.7.

In Figure 2.8, we plot the solution of the equation at times $t = 0.1$, 0.4, 0.9, and 2.0 Gyr for $f = 0.1$ together with the temperature profile obtained in the SPH simulations. The results of the numerical simulations best correspond to the solution of Eqn. (2.18) for $t \sim 0.5 - 0.7\,\mathrm{Gyr}$. For comparison, the ratio of the cloud radius to the flow velocity at infinity is $R/U \sim 1.5 \times 10^8$ yr, while t_s evaluated from the velocity profile obtained in the simulations is $t_s = \left(\frac{\mathrm{d}v_r}{\mathrm{d}r}\right)^{-1} \approx 5 \times 10^8$ yr. The difference in the

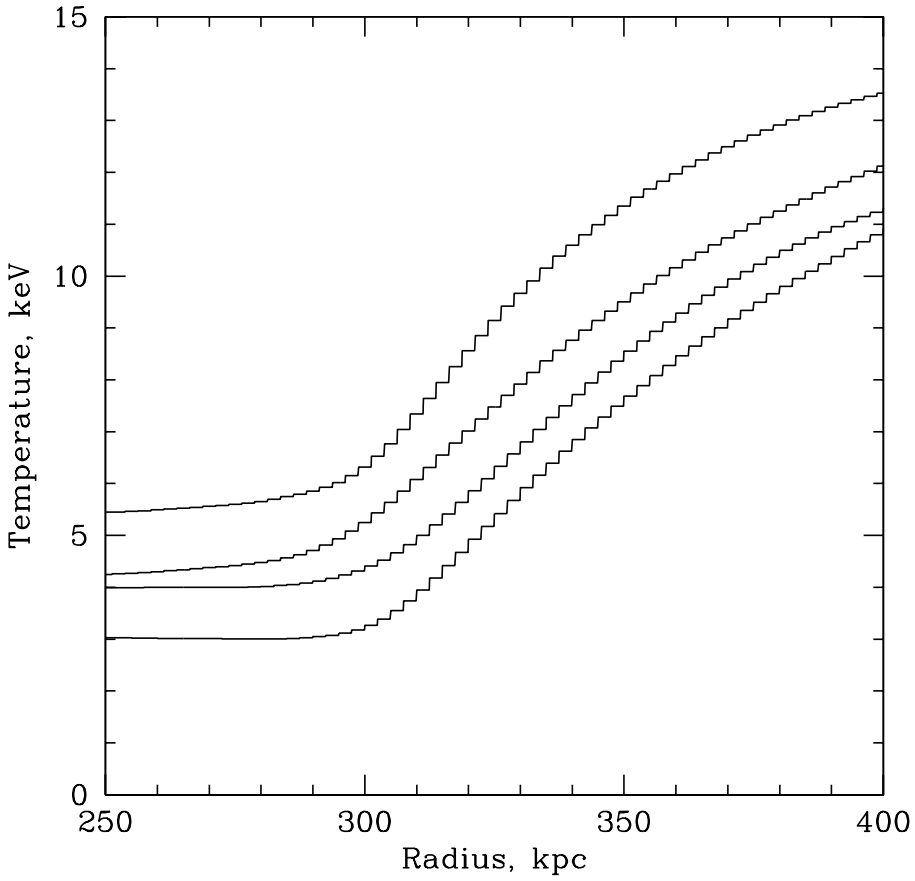

Figure 2.6: Temperature profiles along the symmetry axis of the cloud after $t = 0.2$, 0.4, 0.8 and 1.3 Gyr since the start of the simulations. The conduction suppression coefficient was set to $f = 0.1$. The distance is measured from the centre of the cloud. In order to compensate for the gradual changes in the interface shape, each profile was shifted along the X-axis so that the rising part of the temperature profile has the same abscissa for all curves.

estimated width of the front based on the R/U ratio compared with a more detailed treatment of the velocity field is of order 2. This discrepancy (for our numerical setup) is largely caused by i) the drop of the velocity at the shock and ii) differences between the velocity field obtained in the simulations and that in potential flows of incompressible fluids, as considered in Section 2.2.2. Of course, Eqn.(2.18) by itself is only a crude approximation of the problem. Nevertheless, even our simplest estimate predicts the width of the interface within a factor of 2 of the value derived from direct numerical simulations.

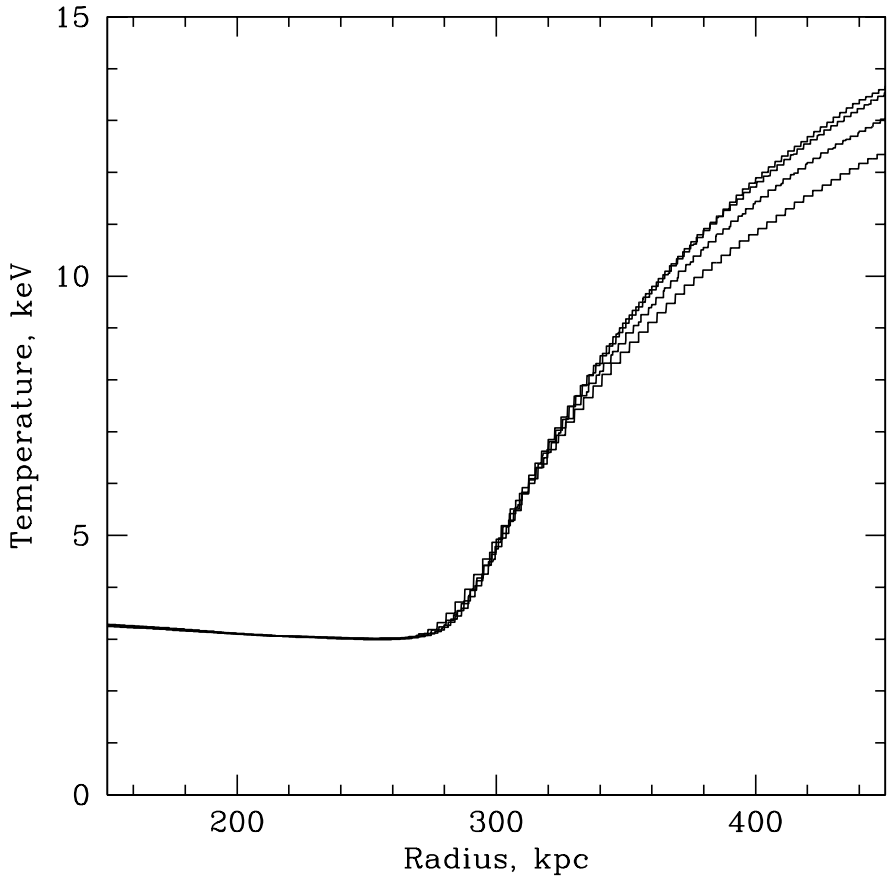

Figure 2.7: Temperature profiles at 1.3 Gyr for $f = 0.1$ along directions making an angle of 0, 15, 30, or 45 degrees with respect to the symmetry axis of the cloud (see also Fig. 2.2).

Note also that because of the expansion of the heated gas, the actual contact discontinuity does not necessarily exactly coincide with the "visible" boundary of the cool cloud. Indeed, colder gas of the cloud expands while the hotter ambient gas contracts, shifting the discontinuity away from the cloud centre. At the same time, the sharpest edge will be observed in places where the temperature gradient is large. If the gas on the two sides of the contact discontinuity has different abundances of heavy elements then the true position of the contact discontinuity can be determined from the abundance gradient. This exercise however requires data of very high quality.

We thus find that an order of magnitude estimate of the width of a spherical cold

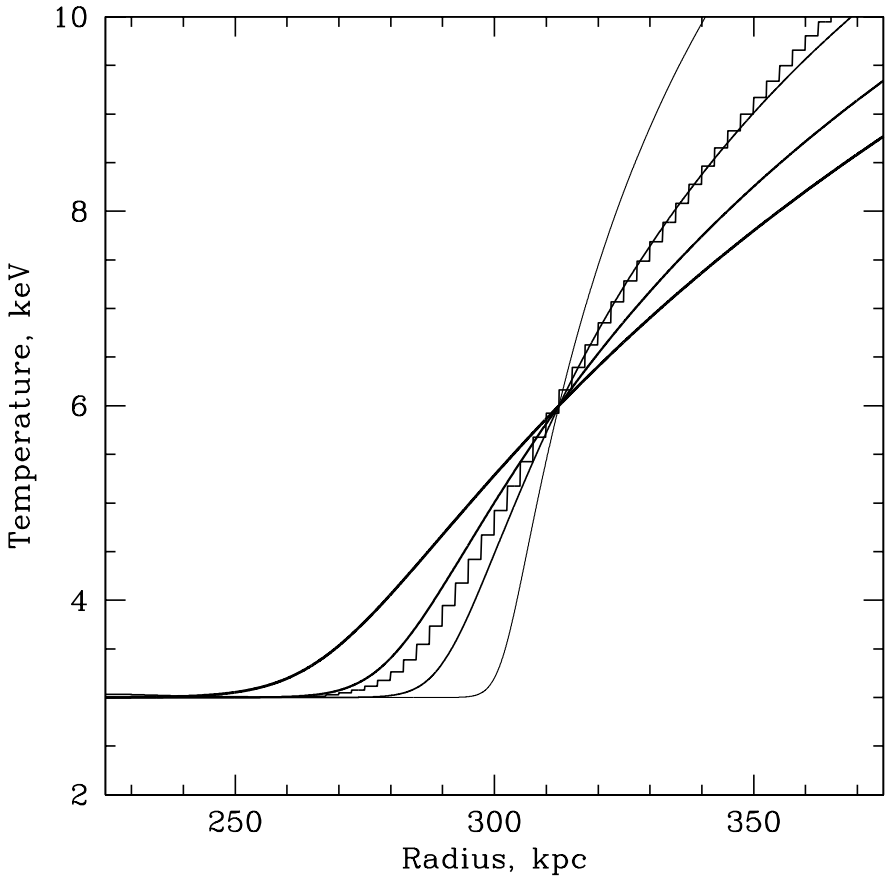

Figure 2.8: Comparison of the temperature profile along the symmetry axis of the cloud (for $f = 0.1$) obtained in numerical simulations (histogram) and obtained from equation (2.18) for $t_s = 0.1$, 0.4, 0.9, and 2.0 Gyr.

front can be written as

$$\Delta r \approx \delta \sqrt{\frac{2}{3} D \frac{R}{U}} = \delta \sqrt{\frac{2}{3} \frac{\gamma - 1}{\gamma} \frac{\mu m_p}{\rho} \frac{f k_0}{k_B} \frac{R}{U}}, \tag{2.19}$$

where the factor δ accounts for all departures introduced by the approximations involved in our simplest model considered in Section 2.2.2. Based on our numerical simulations we have $\delta \sim 0.5$. Plugging in fiducial values for the A3667 cluster (Vikhlinin et al., 2001) one gets:

$$\Delta r \approx 40 \left(\frac{\delta}{0.5} \right) f^{0.5} T_5^{5/4} R_{300}^{0.5} U_{1400}^{-0.5} N_{0.002}^{-0.5} \ \text{kpc}, \tag{2.20}$$

where $T_5 = \frac{T}{5\,\mathrm{keV}}$, $R_{300} = \frac{R}{300\,\mathrm{kpc}}$, $U_{1400} = \frac{U}{1400\,\mathrm{km\,s^{-1}}}$, and $N_{0.002} = \frac{n_e}{2\times10^{-3}\,\mathrm{cm^{-3}}}$.

This value is a factor of ~ 8 larger than the upper limit for the interface width derived from Chandra observations. If this discrepancy is solely caused by a suppression of thermal conduction, then the factor f has to be less than 1.5×10^{-2}. Note that the mean free path is $\lambda \sim 4\ T_5^2 N_{0.002}^{-1}\,\mathrm{kpc}$ (e.g. Sarazin, 1986), which is smaller than the interface width evaluated for $f = 1$. If the effective mean free path of electrons scales linearly with $f = k/k_0$ (while the interface width $\Delta r \propto \sqrt{f}$) then for all $f < 1$ the width of the interface will remain larger than the mean free path. Therefore our assumption of unsaturated heat flux remains valid. For the observed cold front in A3667 the effective mean free path of electrons should therefore be factor $f = 1.5 \times 10^{-2}$ smaller than in unmagnetized plasma.

However, we caution that magnetic fields are likely playing a role in the structure of the interface as suggested by theoretical arguments (e.g. Vikhlinin et al., 2001, Lyutikov 2006) and numerical simulations (e.g. Asai 2004, 2005). Particularly important is the stretching of the field lines along the interface, which can suppress heat conduction across the front or even affect the hydrodynamical stability of the interface. Note that the heat conductivity depends strongly on the topology of the magnetic field since the electron Larmor radius is some 10 orders of magnitude smaller than the characteristic length scales of the problem for typical magnetic field strengths at the micro-Gauss level.

We note that the interface developing in our SPH simulations may also be stabilized to some extent against small-scale fluid instabilities by numerical effects. Across strong density discontinuities, SPH has been found to produce spurious pressure forces that may suppress small wavelength Kelvin-Helmholtz instabilities (Agertz et al. 2006). This effect is equivalent to a small surface tension and mimics the stabilizing influence expected from an ordered magnetic field across the front. However, better numerical resolution weakens this effect and should allow ever smaller wavelengths to grow.

2.5 Conclusions

We have shown that in the presence of thermal conduction the width of the interface separating hot gas flowing past a cooler gas cloud (a "cold front" in clusters of galaxies) can be estimated from the size R of the cloud, the velocity U of the gas and the effective thermal conductivity. The structure of the interface is established over a period of time $\sim R/U$, while the subsequent evolution is much slower. Moreover, the width of the interface is approximately constant along the front. We made an illustrative 2D simulations of an unmagnetized plasma flow past a colder cloud with gas densities and temperatures characteristic for the observed cold fronts. While being very idealized, the simualtions do show that the width remains approximately constant when the gas compressiblity and the temperature dependence of the

conductivity is accounted for.

This implies that one can use much of the visible part of the interface in order to assess the effective thermal conductivity of the gas. For the cold front in Abell 3667, the estimated width of the interface is $40 f^{0.5}$ kpc, where f is the conduction suppression coefficient (relative to the Spitzer-Braginskii value). This factor f has to be smaller than 0.015 in order to reproduce the observed limits on the width of the interface. This result is consistent with previous suggestions that magnetic fields play an important role in providing thermal isolation of the gases separated by the cold front. The idealised description of the interface presented here provides a useful method for estimating the effective gas conductivity from observations of clusters of galaxies.

Bibliography

[1] Acreman, D. M., Stevens, I. R., Ponman, T. J., & Sakelliou, I. 2003, MNRAS, 341, 1333

[2] Agertz et al. 2006, astro-ph/0610051

[3] Asai N., Fukuda N., & Matsumoto R. 2004, ApJL, 606, L105

[4] Asai N., Fukuda N., & Matsumoto R. 2005, Advances in Space Research, 36, 636

[5] Asai, N., Fukuda, N., & Matsumoto, R. 2007, ArXiv Astrophysics e-prints, arXiv:astro-ph/0703536

[Batchelor 1967] Batchelor G.K., An Introduction to Fluid Dynamics, CUP, Cambridge, 1967

[6] Bialek, J. J., Evrard, A. E., & Mohr, J. J. 2002, ApJL, 578, L9

[7] Braginskii S.I., in Reviews of Plasma Physics, edited by Leontovich M.A. (Consultants Bureau, New York, 1965)

[8] Churazov E., & Inogamov N. 2004, MNRAS, 350, L52

[9] Cowie L. L., & McKee C. F. 1977, ApJ, 211, 135

[10] Ettori S., Fabian A. C., 2000, MNRAS, 317, L57

[11] Heinz S., Churazov E., Forman W., Jones C., & Briel U. G. 2003, MNRAS, 346, 13

[12] Jubelgas M., Springel V., & Dolag K. 2004, MNRAS, 351, 423

[13] Landau L.D. & Lifshitz E.M., 1959, Fluid Mechanics (London: Pergamon).

[14] Lamb H.,1932, Hydrodynamics (New York: Dover).

[15] Lyutikov M. 2006, MNRAS, 373, 73

[16] Markevitch M., et al. 2000, ApJ, 541, 542

[17] Markevitch M., & Vikhlinin A. 2007, to appear in Physics Reports

[18] Mathis H., Lavaux G., Diego J. M., Silk J., 2005, MNRAS, 357, 801

[19] Nagai D., & Kravtsov A. V. 2003, ApJ, 587, 514

[20] Narayan, R., & Medvedev, M. V. 2001, ApJL, 562, L129

[21] Spitzer L. 1962, Physics of Fully Ionized Gases, New York: Interscience (2nd edition), 1962

[22] Springel V., 2005, MNRAS, 364, 1105

[23] Takizawa M., 2005, ApJ, 629, 791

[24] Vikhlinin A.,

[25] Tittley E. R., Henriksen M., 2005, ApJ, 618, 227 Markevitch M., & Murray S. S. 2001, ApJ, 551, 160

[26] Vikhlinin A., Markevitch M., & Murray S. S. 2001, ApJL, 549, L47

3 Does heating by AGN shocks affect abundance profiles in galaxy clusters?

submitted to Mon.Not.R.Astron.Soc.

F. Xiang, E. Rudometkin, E. Churazov, W. Forman and H. Böhringer

Abstract

We evaluate the impact of gas shock heating by a central AGN in M87 on the radial distribution of heavy elements. The propagation of a shock creates an inverted entropy profile and the subsequent rearrangement of the gaseous atmosphere transports metal rich gas from the central region to larger radii. We show that for the parameters of the relatively weak shock, recently found in M87, the abundance profile is not strongly affected by the redistribution of the shock heated gas (except for the very central region). At the same time, the energetics of the source is fully sufficient to broaden the metal distribution to match the observations, strongly suggesting that mechanisms other than direct shock heating must operate in cluster cores. The absence of a very strong abundance peak at the very center of M87 suggests that the central AGN produces frequent (every few 10 Myr) and relatively weak outbursts, rather than rarer (every few 100 Myr) and an order of magnitude more powerful events.

3.1 Introduction

X-ray spectroscopy is routinely used to determine the metallicity of the hot gas in galaxy clusters and groups. The gas metallicity contains the record of metals produced by various stellar generations which are then injected into the hot medium by supernova explosions and stellar winds. The gas metallicity is a particularly important diagnostic for cool core clusters whose heavy metal abundances are strongly peaked at the center (e.g. De Grandi et al. 2004; Böhringer et al. 2004). These clusters always have a very bright galaxy (BCG) dwelling in their centers, which makes the stars in BGs a prime candidate for producing the peaked abundance profiles[1]. The total amount of metals, in particular - iron, in cool cluster cores seems to be consistent with this assumption (e.g., Böhringer et al. 2004). The observed distribution of iron is, however, broader than the light distribution of the central galaxy. This suggests that the gas does not form a perfectly static atmosphere, but is instead involved in motions, that transport metals to larger radii. All cool core clusters contain a supermassive black hole (an AGN) in the BCG at the cluster center which is believed to be the source of energy for the cooling gas (e.g. McNamara & Nulsen, 2007 and references therein). AGN activity is also a natural candidate for generation of the gas motions and the metal distribution has been used to constrain the AGN/gas interactions (e.g., Rebusco et al. 2005, 2006; Roediger et al. 2007; Heath, Krause & Alexander 2007; David & Nulsen 2008).

Here we consider the impact of AGN-generated shock heating on the metal distribution in cool core clusters. A shock, driven by an AGN outburst, creates an inverted entropy profile in cluster gaseous atmospheres. The subsequent gas redistribution causes highly enriched gas from the core to move towards larger radii. Motivated by the accurate determination of the shock parameters in M87 using long Chandra observations (Forman et al. 2005, 2007, 2008), we focus on M87 and evaluate the efficiency of this redistribution process.

3.2 Initial conditions: M87 density and temperature profiles

For initial conditions, we used the electron density n_e and temperature T_e profiles derived from long Chandra observations of M87 (Forman et al. 2008, Churazov et

[1] Ram-pressure stripping is another mechanism, which is often discussed in relation to centrally concentrated abundance profiles (see Schindler & Diaferio, 2008 and references therein). We do not consider ram-pressure stripping here. This is at least partly justified since we concentrate on the particular case of a very large elliptical galaxy M87, which strongly dominates its environment up to a distance of ∼100 kpc.

al. 2008). Namely

$$n_e = 0.22 \times \left[1 + \left(\frac{r}{r_c}\right)^2\right]^{-\frac{3}{2}\beta} \quad \mathrm{cm}^{-3}, \tag{3.1}$$

where $\beta = 0.33$ and $r_c = 0.93$ kpc, and

$$T_e = 1.55 \times \left[1 + \left(\frac{r}{10.23 \text{ kpc}}\right)^2\right]^{0.18} \quad \mathrm{keV}. \tag{3.2}$$

These expressions describe reasonably well the best fitting parameters of the deprojected Chandra spectra over the range of radii from ∼1 kpc up to ∼40 kpc, and broadly agree with the XMM-Newton data (Matsushita et al. 2002). Note, however, that deprojected Chandra spectra were approximated by a single temperature APEC model and the best fitting parameters may be subject to various biases in the central region where multi-temperature gas is present. Another caveat is that the gas in M87 is already disturbed by the shock and bubbles of relativistic plasma (e.g. Forman et al. 2005, 2007), but we nevertheless use the fits to the observed profiles as the "pre-outburst" initial conditions for subsequent simulations of the shock propagation. In future work, we will address this issue with a full 3D simulation of the outburst in the M87 atmosphere.

3.3 Production of metals

Metals in elliptical galaxies, dominated by old stellar populations at the present epoch, are produced by SNIa explosions and winds of evolved stars. We assume that the metal production rate follows the optical light distribution of the galaxy. Any possible dependencies of supernovae rates or stellar wind metallicities as a function of radius are ignored. For the metal production rate we use a similar prescription to that of Böhringer et al. (1994) and Rebusco et al. (2006; see references therein). For the SNIa rate we used the latest data of Mannucci et al. (2008) for early type galaxies in clusters: 6.6×10^{-14} $\mathrm{yr}^{-1}\mathrm{M}_{\odot}^{-1}$ (normalized per unit solar mass of the stellar population) and assume that each supernova yields 0.7 $\mathrm{M}_{\odot}$ of iron to the ICM. For the stellar mass loss rate, we use the normalization of Ciotti et al. (1991) for the 10 Gyr old stellar population: $\dot{\zeta} = 2.5 \times 10^{-11}$ $\mathrm{M}_{\odot}\mathrm{yr}^{-1}\mathrm{L}_{\odot,\mathrm{B}}^{-1}$ (per unit B-band stellar luminosity). We assume that iron comprises a fraction 2.8×10^{-3} of the stellar mass loss. For simplicity we assume that both SNIa and stellar mass loss scale with time as $\left(\frac{t}{10 \text{ Gyr}}\right)^{-1}$, where t is the age of the stellar population (by assumption with a present age of $t = 10$ Gyr). With these prescriptions and for a stellar mass of M87

of $M_* = 2.0 \times 10^{11}$ M$_\odot$ and a B-band luminosity of $L_B = 6.4 \times 10^{10}$ $L_\odot$, the total iron enrichment rate is

$$\dot{\zeta}_{Fe} = 1.4 \times 10^{-2} \left(\frac{t}{10 \text{ Gyr}} \right)^{-1}, \quad M_\odot \text{ yr}^{-1}, \tag{3.3}$$

which accounts for SNIa explosions and stellar winds. The stellar wind mass loss rate is:

$$\dot{\zeta} = 1.6 \left(\frac{t}{10 \text{ Gyr}} \right)^{-1}, \quad M_\odot \text{ yr}^{-1}. \tag{3.4}$$

With these definitions, the iron abundance in the gas supplied by stars is

$$z_{Fe} \approx \frac{\dot{\zeta}_{Fe}}{\dot{\zeta}} \frac{1}{A_{Fe} \times z_{Fe,\odot}} = 5.3, \tag{3.5}$$

relative to the solar photospheric abundance. In the above expression $A_{Fe} = 56$ is the atomic weight of iron and $z_{Fe,\odot} = 2.95 \times 10^{-5}$ is the Solar abundance of iron according to Lodders (2003) (see also Asplund et al. 2000). This value sets the maximum abundance which can be reached under the above assumptions[2]. As long as the abundance is lower than this value, the supply of hydrogen by stellar winds can be neglected in the estimates (as we describe below). The high value of the iron abundance predicted by eq.3.5 contrasts with X-ray observations of elliptical galaxies – the problem known in the literature as the "iron discrepancy" (e.g. Renzini et al., 1993, Arimoto et al., 1997). While lowering the SNIa rate and/or the iron mass per explosion can partly remedy the discrepancy, this decrease may, in turn, exacerbate the problem of producing enough iron by cD galaxies in the cores of rich clusters (see iron mass estimates in Boehringer et al. 2004).

The initial radial distribution of iron $\dot{\zeta}(r)$, produced by stars and SNe, should follow the light distribution of the galaxy, modeled as a Hernquist profile (Hernquist 1990). Thus, the iron production rate per unit volume is:

$$\dot{\zeta}_{Fe}(r) = \frac{\zeta_{Fe} M_*}{2\pi} \frac{a}{r} \frac{1}{(r+a)^3}, \tag{3.6}$$

where $a = \frac{R_{eff}}{1.8153}$. For M87 we set $R_{eff} = 7.8$ kpc. The observed light distribution in M87 (e.g. Romanowsky & Kochaneck 2001) is slightly more peaked than the Hernquist profile with these parameters in the inner $\sim 30''$. Since we are mostly

[2]We note that for another popular choice of Solar iron abundance $z_{Fe,\odot} = 4.68\ 10^{-5}$ (Anders and Grevesse, 1989) the abundance, predicted by eq.3.5 drops from 5.3 to 3.3. This value can be further decreased by another ∼30% if one assumes that an SNIa explosion on average produces $0.5 M_\odot$ of iron instead of 0.7.

interested in the gas and metal distributions at larger radii, this minor difference does not affect our results.

The M87 light distribution is much more concentrated than the gas density distribution. Therefore, the production of metals in a static atmosphere will lead to a peaked abundance profile. As shown in Fig.3.1, the expected cumulative abundance profile after a time interval Δt in a static atmosphere is more sharply peaked than the observations. The cumulative abundance was evaluated as the ratio of the amount of iron produced within a sphere of radius R during a time Δt to the total amount of hydrogen within the same sphere. This ratio is normalized by the solar abundance of iron, i.e.,

$$z_{Fe}(R) \approx \frac{\int_0^R \dot{\zeta}_{Fe}(r)\ 4\pi r^2\ dr}{\int_0^R n_e(r)\ 4\pi r^2\ dr} \frac{\frac{n_H}{n_e}}{A_{Fe} \times z_{Fe,\odot}} \times \Delta t, \tag{3.7}$$

where the hydrogen to electron density ratio is given by $\frac{n_H}{n_e} = 0.827$. This estimate ignores the fact that the maximum abundance which can be provided by the enrichment process, with the above parameters, is limited to a maximum value of 5.3 (eq. 5 above).

3.4 Shock model

To model the gas heating by an AGN driven shock, we used the Lagrangian one-dimensional code (as in Forman et al. 2008). The initial density and temperature profiles were set according to equations 3.1 and 3.2. A static gravitational potential $\varphi(r)$ was calculated by requiring the initial density and temperature profiles to satisfy the hydrostatic equilibrium equation. The gas adiabatic index was set to 5/3.

Following Forman et al. (2008), we characterize the AGN outburst with two parameters: total energy E_0 and duration Δt. The AGN power as a function of time is described by a double θ function:

$$L_{AGN}(t) = \begin{cases} 0 & t < 0 \\ \frac{E_0}{\Delta t} & 0 < t < \Delta t \\ 0 & t > \Delta t \end{cases} \tag{3.8}$$

We model the radial distribution of energy deposition (per unit volume) as a power law function of radius:

$$h(r,t) = L_{AGN}(t) \frac{r^{-\alpha}}{\int_0^{R_{AGN}(t)} r^{-\alpha}\ 4\pi r^2 dr}, \tag{3.9}$$

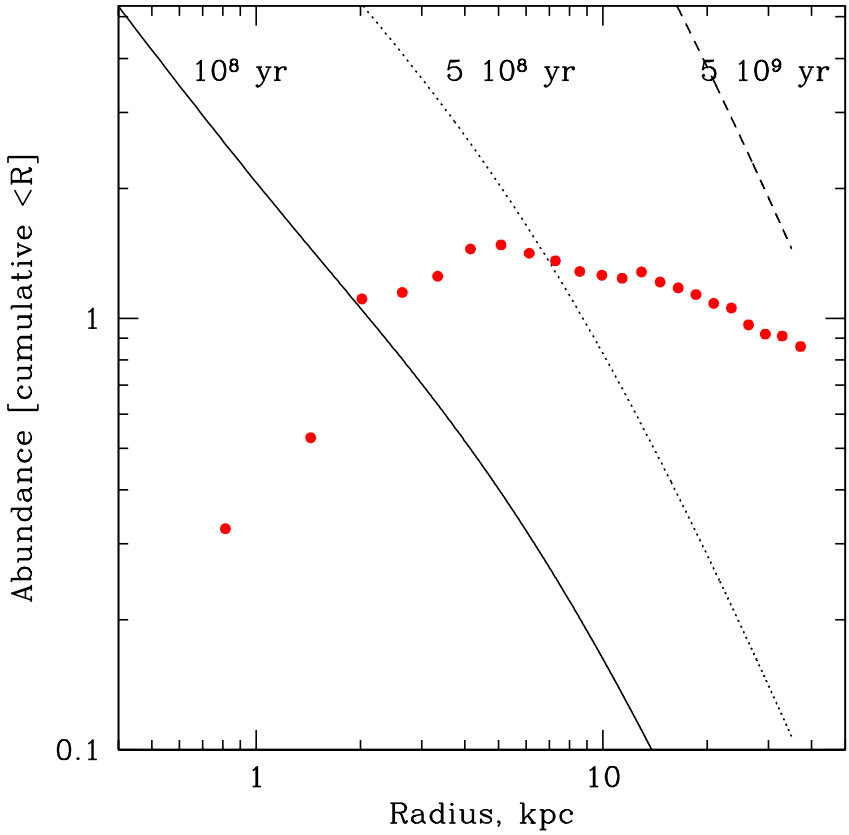

Figure 3.1: The expected abundance profile, if metals are deposited into a static atmosphere for 10^8, 5×10^8 and 5×10^9 years. The maximum abundance which can be produced in our model is 5.3 (corresponding to the top of the plot). For comparison the cumulative abundance derived from the 1T APEC fits to the deprojected Chandra data is shown with red circles. Note that a bias due to the presence of multi-temperature plasma (e.g. Buote 2000) may be very significant in the central 5 kpc ($1'$) region and 1T best fit values may not reflect the true abundance profile here (e.g., Matsushita et al. 2002).

Thus, the energy is deposited in a few central cells $r < R_{AGN}(t)$: the internal energy in the cells is increased at each time step according to the above equation 3.9. Initially the outer radius of the region used for energy deposition is $R_{AGN}(0)$ =0.5 kpc. As the radii of the cells grow, the injection region grows accordingly. This was done to mimic the situation when the AGN is inflating a bubble of relativistic plasma at the center with internal sound crossing time much smaller than the characteristic time of

the bubble expansion. The value of α was (arbitrarily) set to 0.5 in the simulations. The properties of the final density and temperature profiles only weakly depend on the particular value of α (as was verified by varying α from 0 to 1).

Guided by the fiducial values derived for the M87 shock from Chandra observations (Forman et al. 2007, 2008): $E_0 \sim 5 \times 10^{57}$ ergs and $\Delta t \sim 2 \times 10^6$ yr, we ran a grid of models with bracketing values of E_0 and Δt. Namely $E_0 = \{5 \times 10^{56},\ 5 \times 10^{57},\ 5 \times 10^{58}\}$ ergs, duration $\Delta t = \{2 \times 10^5,\ 2 \times 10^6,\ 2 \times 10^7\}$ yr - all together nine runs. In the simulations, we follow the shock propagation until the leading front reaches a distance of 30 kpc from the center. By this time the shock has become relatively weak and no longer generates much entropy. The choice of this particular radius (30 kpc) is rather arbitrary but our results are insensitive to the actual value.

The gas density and temperature profiles modified by the shock in each of the 9 runs are shown in Fig.3.2 with colored lines. For comparison, the initial profiles are shown with the black lines. One can easily identify three distinct regions in the profiles modified by the shock:

Region I - the innermost part of the atmosphere, which corresponds to the region where the energy was directly deposited during the simulations (i.e. gas inside $R_{AGN}(t)$). As the gas is directly heated in this region (by design of our simulations) it has very high entropy and, as a consequence, has a high temperature and low density. For M87 (and other cooling flows), a more relevant model could be one in which relativistic plasma is injected by an AGN into the central region, rather than direct heating of the gas. For the purpose of this paper this is not a critical issue, since the initial value of $R_{AGN} = 0.5$ kpc is small enough (much smaller than the galaxy effective radius) that only a small fraction of the gas and metals generated by the galaxy lie in this region. For instance, for a pure Hernquist profile with effective radius of 7.8 kpc, only $\sim$1% of the galaxy light is contained within the central 0.5 kpc. In M87 this fraction can be larger (due to a more peaked light profile near the center), but it is still small.

Region II - intermediate regions between Region I and the shock front. This is the most important region for the purpose of this paper. The gas in this region is heated by the shock propagation. If the shock is strong (due to a powerful and short duration outburst) then the gas is strongly heated. In the opposite case of a weak shock (less powerful and of long duration), the gas in region II is merely displaced by the expanding central Region I, except for a narrow shell immediately adjacent to Region I.

Finally, Region III - is the region outside the leading shock front (i.e. $r > 30$ kpc in Fig.3.2), occupied by undisturbed gas.

The radii separating Regions I and II are visible in Fig.3.2 as almost vertical lines, corresponding to a sharp drop of temperature from values above 3 keV to values below 2 keV. The boundary between Region II and III is by definition at 30 kpc, where the jump in temperature/density is seen.

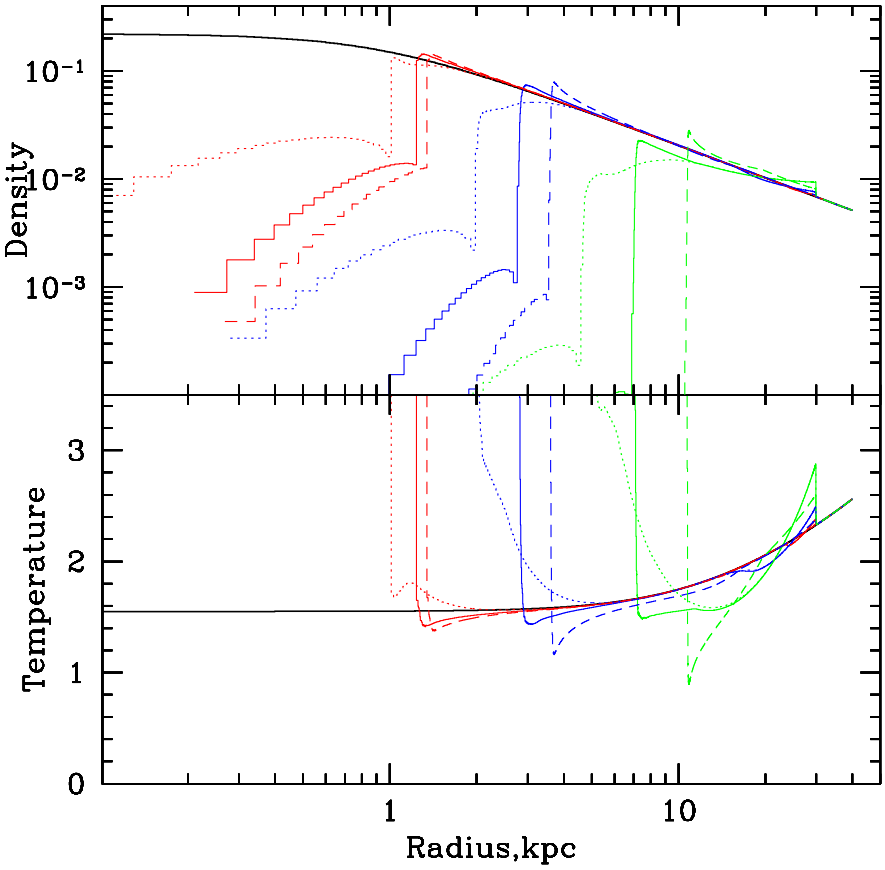

Figure 3.2: Density and temperature profiles modified by the outburst of a central AGN. Red, blue and green lines correspond to the outburst energy $E_0 = 5 \times 10^{56}$, 5×10^{57}, 5×10^{58} ergs respectively. Dotted, solid and dashed lines correspond to outburst duration $\Delta t = 2 \times 10^5$, 2×10^6 2×10^7 yr respectively. Snapshots shown correspond to the time when the leading front of the shock reaches a distance of 30 kpc distance from the center. The black lines show the initial gas density and temperature profiles.

3.5 Entropy and abundance profiles

The gas entropy profiles (to be precise the profiles of the quantity $s(r) = \frac{T_e}{n_e^{2/3}}$) corresponding to the same set of shock models are shown in Fig.3.3. When the energy is released into an initially small volume - a relatively strong shock is driven into the cluster gas and it substantially increases the gas entropy. As the shock propagates

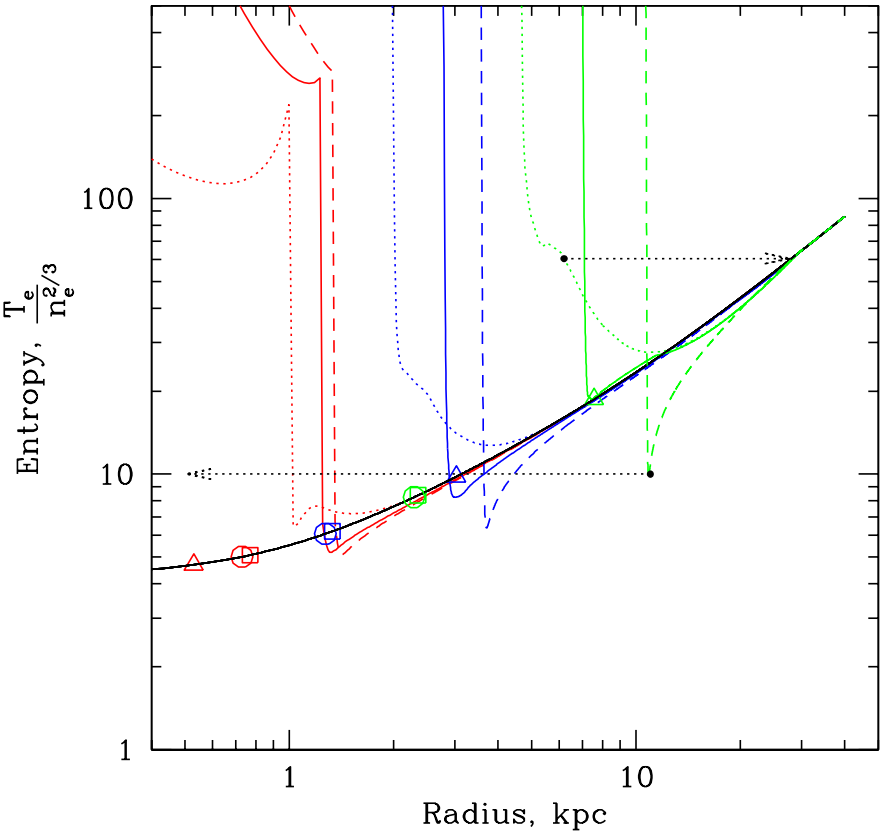

Figure 3.3: Inversion of the entropy profile caused by shock heating of the central region. The colors and line types are coded similarly to Fig.3.2. Two black arrows show schematically that heated gas will move towards large radii, while the lowest entropy gas will sink to the center. For each model the open triangle, circle and square (for $\Delta t = 2 \times 10^5$, 2×10^6 2×10^7 yr respectively) mark the initial radius of the cell which has the lowest entropy at the end of the simulation.

through the gas and weakens (the density profile is less steep than r^{-2}), the shock becomes less efficient at entropy generation. As a result an inverted entropy profile is created, as seen in Fig.3.3. For "short" duration outbursts the entropy increase is more pronounced since such outbursts generate stronger shocks. The corresponding profiles have extended minima. For "long" duration outbursts the gas is merely displaced by expanding Region I (as explained above) and the corresponding profiles are characterized by narrower and deeper minima.

3.6 Rearrangement of the atmosphere and resulting abundance profiles

An atmosphere with an inverted entropy profile (as shown in Fig.3.3) is unstable and must pass through a rearrangement phase which will restore the atmosphere to one with a nondecreasing (with radius) entropy profile. Low entropy gas will tend to sink to the center of the cluster, while high entropy gas will instead move towards larger radii as shown by the dotted arrows in Fig.3.3. After a few dynamical times (few 10^7 yr) the atmosphere will come to a stable equilibrium. Since the dynamical time is short compared to the cooling or enrichment time scales, we assume that for the purposes of studying the evolution of the heavy elements, the rearrangement is instantaneous. The rearrangement process is very complex since gas lumps with different entropies can mix during the gas motion. We will completely ignore these complications and assume that the gas mass distribution over entropy remains unchanged during rearrangement. We also neglect (for the purpose of our simple model) the potential energy released during rearrangement process[3]. Namely we model rearrangement as follows. From our shock simulations, we have the gas mass m_i, iron mass $m_{Fe,i}$ and the entropy s_i for each of the $i = 1, n$ simulated cells. We then rearrange the cells (and associated masses) to produce a stable atmosphere, i.e., entropy increasing with radius (cell index). We now solve the hydrostatic equilibrium equation

$$\frac{1}{\rho}\,\frac{dP}{dr} = -\frac{d\varphi}{dr}, \tag{3.10}$$

with the boundary condition that the pressure at the outer boundary is equal to $P(r_n) = P_{out}$. A similar approach was used by Kaiser & Binney (2003). We start with an initial estimate of the pressure at the center of the cluster P_c and calculate the density of the first cell as $\rho_1 \propto \left(\frac{P_c}{s_1}\right)^{3/5}$. We then integrate eq.3.10 over one cell to get the pressure for the next cell and repeat the procedure for the next cell. The pressure in the outmost shell $P(r_n)$ is compared with P_{out}. If they do not match then P_c is adjusted and the whole procedure repeats until agreement is reached. If the outer boundary is sufficiently far from the region affected by the shock then the behavior of the solution in the inner region does not depend much on the radius r_n used for the outer boundary condition $P(r_n) = P_{out}$. The outcome of this procedure is a new stable configuration for the atmosphere with a known gas mass and iron mass for each shell composing this atmosphere.

Since the shock preferentially heats the inner regions, where most of metals are produced, the exchange of gas parcels with high and low entropies causes high metal-

[3]While heating certainly occurs during the rearrangement process, we intentionally limit our consideration to the entropy generation at the shock front only.

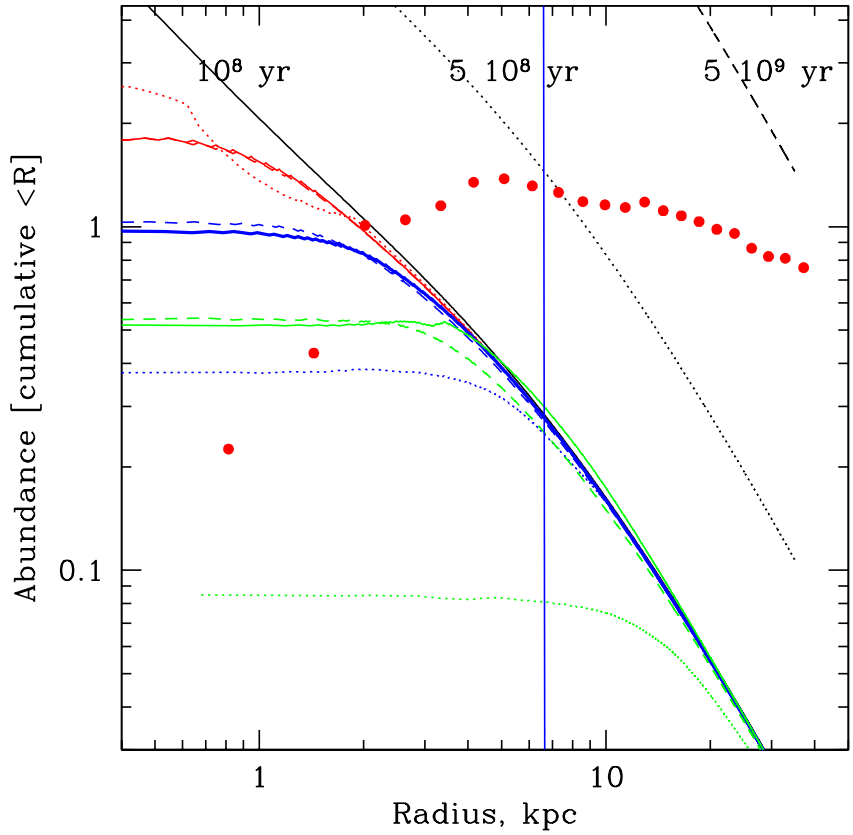

Figure 3.4: Modification of the cumulative abundance profiles after the atmosphere restores a stable configuration (entropy increasing outward, as described in the text). The thick solid blue curve corresponds to the best fitting shock parameters ($E_0 \sim 5 \times 10^{57}$ ergs and $\Delta t \sim 2 \times 10^6$ yr) for M87 (Forman et al 2007). The blue vertical line shows the $R = 6.6$ kpc radius of the sphere within which the gas can be mixed if the energy $E_0 \sim 5\ 10^{57}$ ergs is used to raise the entropy of the gas inside the sphere to the value characteristic for the gas just outside this sphere. The cumulative abundance profile derived from Chandra data is shown with red points.

licity gas in the very core to be replaced with less metal rich gas from larger radii. The resulting (cumulative) abundance profiles for each of the shock models are shown in Fig.3.4.

3.7 Discussion

3.7.1 Effect of Shock Strength and Outburst Energy

As is clear from Fig.3.4, for all models the abundance profiles develop a characteristic core at the center. The radial extent of the core (and the maximal abundance) is a function of the minimum entropy present in the system after the passage of the shock, which is in turn a function of the outburst energy E_0 and outburst duration Δt. The more powerful and short the outburst, the larger is the core of the abundance profile. From Chandra observations of M87, Forman et al. (2007, 2008) argued that the recent ($\sim$10 Myr old) major outburst was best described by $E_0 \sim 5\ 10^{57}$ ergs and $\Delta t \sim 2\ 10^6$ yr. These parameters correspond to the blue solid line in Fig.3.4. One can see that the radius of the abundance core is only $\sim$1-2 kpc i.e., after a single outburst the metals stay well within the effective radius of the galaxy where they are produced[4]. This rather small impact on the abundance distribution is a direct consequence of a rather "mild" outburst, which does not significantly change the gas entropy (except for a very small region in the center).

The gas cooling time at the center of M87 is $t_{cool,0} \sim 10^8$ yr. It was evaluated as $t_{cool} = \dfrac{5/2(n_e + n_i)kT}{n_e n_i \Lambda(T)}$ using the cooling function $\Lambda(T)$ from Sutherland & Dopita (1993) with $T_e = 1.55$ keV, $n_e = 0.2$ cm^{-3} and Solar metallicity. Thus, to avoid a cooling catastrophe the characteristic time between outbursts t_{rep} has to be shorter than the cooling time, i.e., $t_{rep} \lesssim t_{cool,0} = 10^8$ yr.

On the other hand the cooling time at 50 kpc is $\sim 10^{10}$ yr and the total radiative losses of the gas inside the same radius are $L_{cool} \sim 1.3 \times 10^{43}$ erg s^{-1}. Assuming that this 50 kpc region is a "cooling flow region" in M87 and radiative losses inside 50 kpc are replenished by AGN outbursts (with an efficiency of converting outburst energy to heat close to 1 as suggested by Fig.3.5), we can estimate the energy required from a single outburst

$$E_1 = L_{cool} \times t_{rep} = 4 \times 10^{58} \left(\frac{t_{rep}}{10^8 \text{ yr}}\right) \text{ ergs}. \tag{3.11}$$

Such outbursts would have stronger impact on the abundance profile. The Chandra data (Forman et al. 2007, 2008) suggest that an order of magnitude less powerful outburst occurred about 10^7 years ago. If such outbursts are typical for M87 then a more plausible scenario would be ~ 10 times more frequent outbursts, i.e., $t_{rep} \approx 10^7$ yr $\approx 0.1 \times t_{cool,0}$ and ~ 10 times less powerful outbursts. The shock heating from these weak outbursts would have little impact on the abundance profiles outside $\sim$2 kpc.

One can also use the abundance peak (or lack of a peak) at the center of M87 to constrain the interval between the outbursts t_{rep}. Indeed in 10^8 years the metal

[4]The impact of multiple outbursts is discussed later

injection by stars increases the abundance at 1 and 2 kpc distances from the galaxy center by 2 and 1 Solar values respectively (see Fig.3.1 or 3.4). Thus, the absence of a very sharp abundance peak in the very core of M87, by itself, means that outbursts must occur often. If one could reliably measure the abundance difference at two radii (1 and 2 kpc) then the expected difference in abundances will be $\Delta z \sim \left(\frac{t_{last}}{10^8 \text{ yr}}\right)$, where t_{last} is the elapsed time since the latest major outburst. There are two caveats associated with this estimate. First, the central part of M87 is exactly the region where reliable abundance determination is observationally difficult. Second, the same region is currently undergoing an outburst and any estimate cannot be very accurate. Nevertheless, the mere absence of an abundance spike in the very core of M87 is best explained by frequent (and weak) outbursts.

Qualitatively a similar conclusion was reached by Simionescu et al. (2008) based on the analysis of XMM-Newton observations of M87. They measured the abundance of iron and other elements in the cool gas which is believed to be enriched by stars near the very core of M87 and then uplifted to larger radii by buoyant bubbles of relativistic plasma. From measured abundances, Simionescu et al. (2008) concluded that the enrichment time of the cool gas (analogous to the t_{rep} above) is somewhere between 30 and 100 Myr.

3.7.2 Energetically more efficient mixing

The above model assumes that entropy generation (i.e., heating) occurs exclusively at the shock fronts. By design of our simulations, the subsequent rearrangement of the gas layers conserves entropy and the excess potential energy released during the rearrangement process is neglected. It is interesting to consider a more energetically efficient mixing scenario when the available energy E_0 is used to create a flat entropy profile within a sphere with radius R_{mix}. The resulting distribution will be neutrally stable and mixing can proceed over the whole volume of the sphere. We can calculate the energy needed to *instantaneously* heat the gas at each radius to produce a flat entropy profile to a radius R_{mix}:

$$E_0 = \int_0^{R_{mix}} \frac{nkT}{\gamma - 1} \frac{s(R_{mix}) - s(r)}{s(r)} \, 4\pi r^2 dr. \tag{3.12}$$

Solving the above equation for R_{mix} we find that for $E_0 \sim 5 \times 10^{57}$ ergs, a flat entropy profile can be generated within $R_{mix} = 6.6$ kpc. Except for the factor $\frac{s(R_{mix}) - s(r)}{s(r)}$, the expression under the integral is the gas thermal energy. For realistic conditions, the the dominant contribution to the integral comes from the radial range $r \sim R_{mix}$. The factor $\frac{s(R_{mix}) - s(r)}{s(r)} \sim 1$ and for simple estimates it can be dropped from eq.3.12. For M87 (over the range of E_0 of interest here, i.e., for $E_0 \sim 5\ 10^{57}$ ergs),

omitting this entropy factor introduces an error of less than a factor of 2 in R_{mix} and changes R_{mix} from 6.6 kpc to 4.6 kpc. The above estimate essentially says that to mix the gas within a radius R_{mix} one needs to deposit an amount of energy comparable to the gas thermal energy within a volume ${R_{mix}}^5$

The resulting radius R_{mix} over which the gas is mixed, is much larger than the 1-2 kpc core in the abundance distribution produced by shock heating for our fiducial set of outburst energies and durations. We emphasize that this "inefficiency" of gas mixing is not due to a large fraction of outburst energy escaping from the cooling flow region with the outgoing shock/sound wave. In fact, for the outburst parameters favored by the Chandra data, only a small fraction, less than 20 percent (see Fig.3.5), is carried away from the central 30 kpc region by the outgoing shock. Instead, for a moderately powerful and long duration outburst ($E_0 \sim 5\ 10^{57}$ ergs and $\Delta t \sim 2\ 10^6$ yr), the bulk of the energy goes into the enthalpy of a central, very high entropy volume/cavity. In the mixing scenario described by eq.3.12, the same amount of energy E_0 is spread over a much larger volume allowing for large masses of gas to be mixed. The very same arguments imply that not only gas mixing, but also gas heating by shocks is inefficient. As discussed by Churazov et al. (2001, 2002; see also Begelman 2001; Nulsen 2006), the energy stored as enthalpy of the central cavity can be used for efficient gas heating during the rise of the buoyant cavity through the cluster atmosphere. The final heating efficiency (entropy generation) in this model is high, but this heating is not directly related to the entropy generation at the front of the original shock. Similarly, one can expect that the same mechanism will increase the mixing efficiency. The mixing induced by jets and buoyant bubbles was, in particular, studied in numerical simulations by Roediger et al. (2007) and Heath et al (2007). They found that jets and bubbles can indeed disperse metals through the ICM.

3.7.3 Toy mixing model

Starting from the assumption that the gas heating efficiency and metal mixing are linked to each other we can build a simple toy model of metal mixing in cluster cooling cores.

Let us assume that the time averaged AGN mechanical power L_{AGN} matches approximately the gas cooling losses integrated over the cooling flow region. For M87 this means $L_{AGN} \sim$ few $\times\ 10^{43}$ ergs s^{-1}. We further assume, along the lines of the arguments presented above, that the gas mixing efficiency induced by the AGN follows eq.3.12. If the AGN was active for a time interval τ, then the gas is uniformly mixed inside a sphere with radius $\Re(\tau)$ such that the gas thermal energy inside the

[5] We stress that in general the above estimate does not correspond to the minimum energy required to mix the gas within a given sphere. This is simply one possible way, not necessarily the most efficient, to promote mixing.

sphere matches the AGN power released during a period τ:

$$\tau \times L_{AGN} = \int_0^{\Re(\tau)} \frac{nkT}{\gamma - 1}\, 4\pi r^2 dr. \tag{3.13}$$

This equation is essentially eq.3.12, where we have omitted the factor $\frac{s(\Re) - s(r)}{s(r)}$ for the sake of simplicity (given the qualitative level of these estimates).

With the above prescription, a short period of AGN activity will cause gas mixing inside a small sphere while a long period of activity mixes the gas in a larger sphere. In particular, during one cooling time the gas inside a cooling radius is mixed. Thus, metals produced about one cooling time ago will be dispersed over the whole cooling flow region, while more recently produced metals are mixed within a smaller sphere. Assuming that the AGN was active for a period of time from t_1 to t_2, the total mass of iron within a sphere with radius R can be evaluated as

$$M_{Fe}(< R) = \int_{t_1}^{t2} dt\; A(t, R), \tag{3.14}$$

where

$$A(t,R) = \begin{cases} \frac{M_{gas}(<R)}{M_{gas}(<\Re(t))} \int_0^{\Re(t)} \dot{\zeta}_{Fe}(r)\, 4\pi r^2 dr & \Re(t) > R \\ \\ 0 & \Re(t) < R \end{cases} \tag{3.15}$$

Here $\Re(t)$ is evaluated using eq.3.13. The expected abundance profiles for different values of the AGN mechanical power are shown in Fig.3.6. For this figure, we set t_1 and t_2 to 0.5 and 10 Gyr respectively. Clearly within our toy model the AGN power of 10^{44} ergs s^{-1} would mix metals over very large regions (perhaps beyond the valid range of the density and temperature profiles used here) resulting in very low metal abundances in the core[6]. An AGN power of 10^{42} ergs s^{-1} would instead produce very little mixing and in the central ∼20-30 kpc the abundance will be ∼5 Solar. An AGN power of order of L_{AGN} = few $\times\, 10^{43}$ ergs s^{-1} yields an abundance level which approximately matches the observations. Therefore, we conclude that in our toy model, a time average energy input of order a few $\times\, 10^{43}$ ergs s^{-1} is needed to explain the M87 abundance profile. This energy input, within a factor of 2 (depending on the definition of the cooling radius), coincides with the gas cooling losses in M87. Given the simplicity and obvious crudeness of our estimates, we conclude that the model is reasonably successful in reproducing the basic characteristics of M87.

[6] One should bear in mind that the gas has been already enriched by SNII explosions during an early phase of cluster/galaxy evolution. The metals produced by SNIa during the subsequent evolution are added to this 'minimum' abundance level which amounts to ∼0.1-0.3 of the Solar metallicity. This minimum level has to be added to the profiles predicted by our model or subtracted from the observed profiles to make the comparison fair. Because of the large uncertainty in the value of the minimum abundance, we do not do this in Fig.3.6 and simply plot the original observed and model profiles.

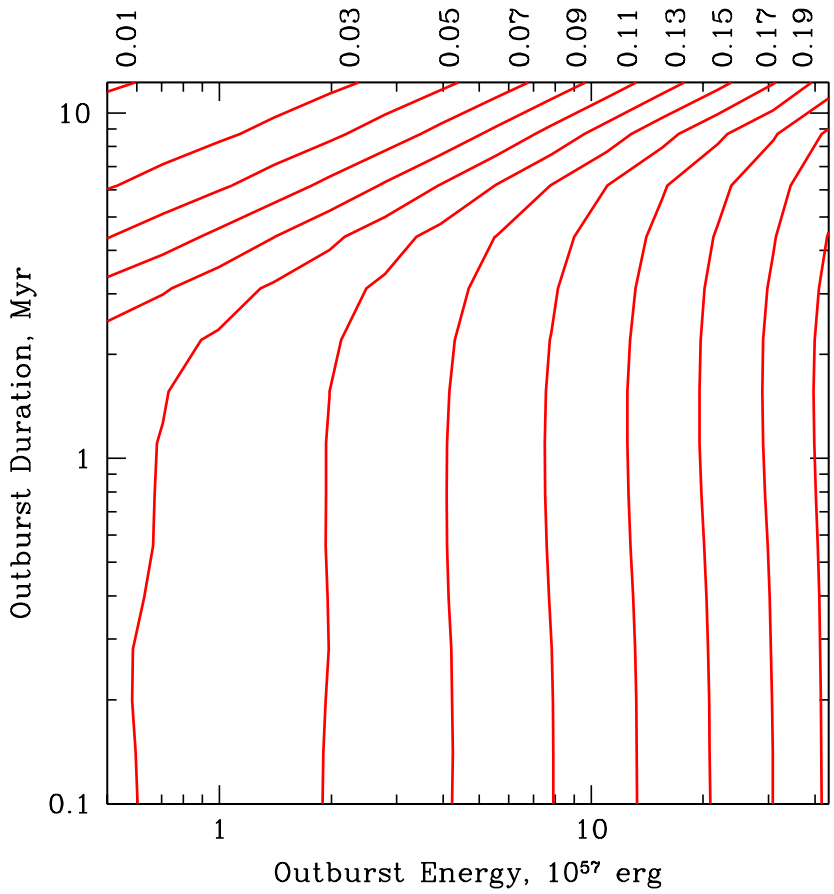

Figure 3.5: The fraction of the outburst energy (contours) escaping from the central 30 kpc region with the expanding shock as a function of the outburst total energy (X-axis) and the outburst duration (Y-axis). The actual fraction associated with each contour is shown by a label at the top of the plot. The energy escaping from 30 kpc region was evaluated by calculating the kinetic energy of the gas at the time when the shock front was at 30 kpc from the center and multiplying this value by 2. This is a crude estimate which assumes that we deal with a simple weak plane wave having total energy twice its kinetic energy.

The comparison of the abundance core of 1-2 kpc expected in a pure shock heating model (for $E_0 \sim 5 \times 10^{57}$ ergs and $\Delta t \sim 2 \times 10^6$ yr) and $R_{mix} = 6.6$ kpc expected from eq.3.12 ($R_{mix} = 4.6$ kpc from eq.3.13) suggests that our toy model is considerably more efficient at metal mixing. An energy of order a few $\times 10^{56}$ ergs would be sufficient to mix the gas inside 1-2 kpc if eq.3.12 or 3.13 applies. Extrapolating this difference in efficiency to the multiple explosions, we can conclude that at least an

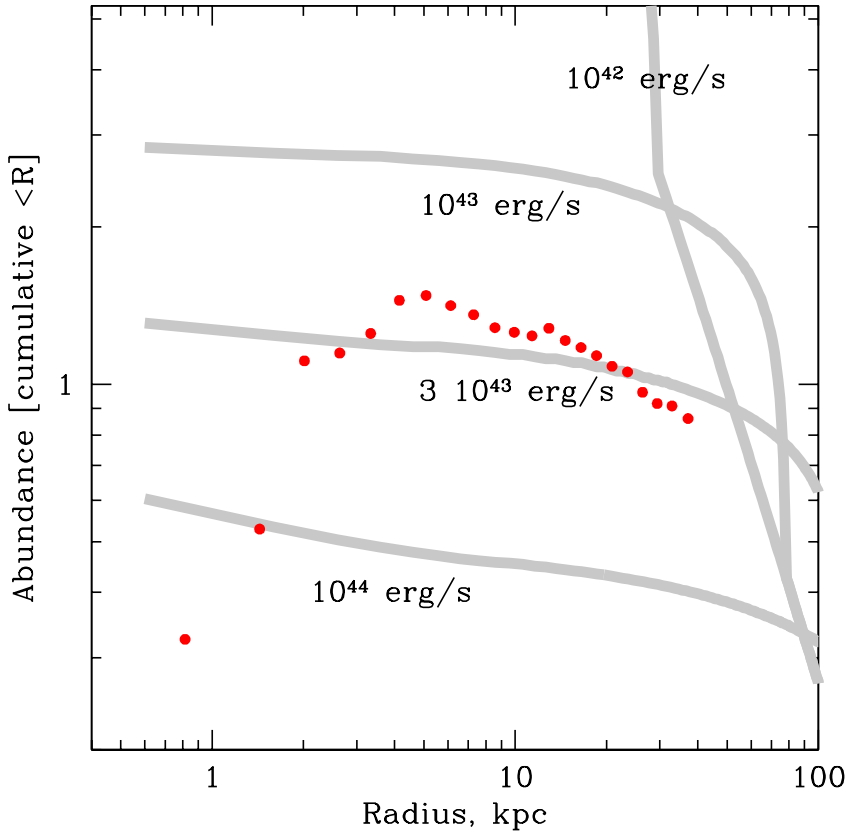

Figure 3.6: Abundance profile in the toy model for different AGN outburst powers. The gray curves are the predicted abundance distributions according to eq.3.14 for $L_{AGN} = 10^{42}$, 10^{43}, 3×10^{43} and 10^{44} erg s^{-1} from top to bottom respectively.

order of magnitude larger time averaged AGN power (few $\times 10^{44}$ ergs s^{-1}) would be needed in M87 to provide mixing that is driven purely by shock heating.

Of course the above toy model cannot even approximately describe the process of metals spreading through the ISM/ICM. The model is built around a single assumption that a deposition of a given amount of energy into the gas leads to the gas mixing within the sphere containing a similar amount of thermal energy. All other complications including gas cooling, physics of gas heating, process of mixing are neglected. Nevertheless, we believe that our toy model can serve as an order of magnitude approximation of a mixing process mediated by bubbles of relativistic plasma which steer the gas during their buoyant rise and simultaneously provide gas

heating and mixing.

3.8 Conclusions

We consider a simple model of metal spreading through the gaseous atmospheres of cool core clusters due to gas shock heating by a central AGN outburst. In particular, for M87, we show that for the outburst parameters derived from the Chandra data (Forman et al. 2007, 2008), the generation of entropy at the shock front by itself does not provide an efficient mechanism for metal transport. However, the energetics of the source are sufficient to spread metals over a large volume (e.g., by entrainment of the metal rich gas or by steering gas motions in the center). The assumption that gas mixing and gas heating are closely related to each other leads to a simple qualitative model. The model assumes that full mixing of the gas within a sphere of a given radius occurs on time scales needed to double the gas thermal energy inside the same sphere. The abundance profile expected in such a simple model demonstrates reasonable similarity to the observed abundance profile in M87 if the time averaged AGN power is of order a few$\times$ 10^{43} ergs s^{-1}. This value agrees well with the value needed to offset the gas cooling losses in M87.

Bibliography

[1] Anders E., Grevesse N., 1989, GeCoA, 53, 197

[2] Asplund M., Nordlund Å., Trampedach R., Allende Prieto C., Stein R. F., 2000, A&A, 359, 729

[3] Begelman M. C., 2001, ASPC, 240, 363

[4] Böhringer H., Matsushita K., Churazov E., Finoguenov A., Ikebe Y., 2004, A&A, 416, L21

[5] Buote D. A., 2000, MNRAS, 311, 176

[6] Cappellaro E., Evans R., Turatto M., 1999, A&A, 351, 459

[7] Churazov E., Brüggen M., Kaiser C. R., Böhringer H., Forman W., 2001, ApJ, 554, 261

[8] Churazov E., Sunyaev R., Forman W., Böhringer H., 2002, MNRAS, 332, 729

[9] Churazov E., Forman W., Vikhlinin A., Tremaine S., Gerhard O., Jones C., 2008, MNRAS, 388, 1062

[10] Churazov E., Forman W., Jones C., Sunyaev R., Böhringer H., 2004, MNRAS, 347, 29

[11] Ciotti L., D'Ercole A., Pellegrini S., Renzini A., 1991, ApJ, 376, 380

[12] De Grandi S., Ettori S., Longhetti M., Molendi S., 2004, A&A, 419, 7

[13] David L. P., Nulsen P. E. J., 2008, arXiv, 802, arXiv:0802.1165

[14] Forman W., et al., 2005, ApJ, 635, 894

[15] Forman W., et al., 2007, ApJ, 665, 1057

[16] Forman W., et al., 2008, ApJ, to be submitted

[17] Heinz S., Churazov E., 2005, ApJ, 634, L141

[18] Heath D., Krause M., Alexander P., 2007, MNRAS, 374, 787

[19] Hernquist L., 1990, ApJ, 356, 359

[20] Kaiser C. R., Binney J., 2003, MNRAS, 338, 837

[21] Lodders K., 2003, ApJ, 591, 1220

[22] Mannucci F., Maoz D., Sharon K., Botticella M. T., Della Valle M., Gal-Yam A., Panagia N., 2008, MNRAS, 383, 1121

[23] Matsushita K., Belsole E., Finoguenov A., Böhringer H., 2002, A&A, 386, 77

[24] Matsushita K., Finoguenov A., Böhringer H., 2003, A&A, 401, 443

[25] McNamara B. R., Nulsen P. E. J., 2007, ARA&A, 45, 117

[26] Nulsen, P. E. J., Jones, C., Forman, W., David, L., McNamara, B., Rafferty, D., Birzan, L., Wise, M., 2006, in Boehringer H., Schuecker P., Pratt G. W., Finoguenov A., eds, Heating vs. Cooling in Galaxies and Clusters of Galaxies. Springer-Verlag, Berlin (astro-ph/0611136)

[27] Rebusco P., Churazov E., Böhringer H., Forman W., 2005, MNRAS, 359, 1041

[28] Rebusco P., Churazov E., Böhringer H., Forman W., 2006, MNRAS, 372, 1840

[29] Roediger E., Brüggen M., Rebusco P., Böhringer H., Churazov E., 2007, MNRAS, 375, 15

[30] Schindler S., Diaferio A., 2008, SSRv, 134, 363

[31] Simionescu A., Werner N., Finoguenov A., Böhringer H., Brüggen M., 2008, A&A, 482, 97

[32] Sutherland R. S., Dopita M. A., 1993, ApJS, 88, 253

4 Conclusions

4.1 Cold fronts and thermal conduction in cluster plasma

Chandra observations of galaxy clusters often show sharp discontinuities in the surface brightness of the hot intra-cluster medium (ICM) emission (Markevitch et al., 2000, Vikhlinin, Markevitch, Murray, 2001, see Markevitch & Vikhlinin 2007 for a review). Most of these structures have lower temperature gas on the brighter (higher density) side of the discontinuity, contrary to the expectation for non-radiative shocks in the ICM. Within the measurement uncertainties, the pressure is continuous across these structures, suggesting that they are contact discontinuities rather than shocks. We have considered a model of a differential gas motion of a hot gas with respect to a colder gravitationally bound gas cloud. In such a situation one expects that ram pressure of the hotter gas strips the outer layers of the colder cloud, exposing denser gas layers and forming a cold front near the stagnation point of the hot flow.

Using SPH simulations of a cold cloud embedded in a hot flow we have shown that in the presence of thermal conduction the width of the interface, separating hot gas from a cooler gas in the cloud (a "cold front" in clusters of galaxies) can be estimated from the size R of the cloud, the velocity U of the gas and the effective thermal conductivity. The structure of the interface is established over a period of time $\sim R/U$, while the subsequent evolution is much slower. Moreover, the width of the interface is approximately constant along the front. We made an illustrative 2D simulations of an unmagnetized plasma flow past a colder cloud with gas densities and temperatures characteristic for the observed cold fronts. While being very idealized, the simulations do show that the width remains approximately constant when the gas compressibility and the temperature dependence of the conductivity is accounted for.

This implies that one can use much of the visible part of the interface in order to assess the effective thermal conductivity of the gas. For the cold front in Abell 3667(Best studied example of a cold front), the estimated width of the interface is $40 f^{0.5}$ kpc, where f is the conduction suppression coefficient (relative to the Spitzer-Braginskii value). This factor f has to be smaller than 0.015 in order to reproduce the observed limits on the width of the interface. This result is consistent with previous suggestions that magnetic fields play an important role in providing thermal isolation of the gases separated by the cold front. The idealized description of the interface

presented here provides a useful method for estimating the effective gas conductivity from observations of clusters of galaxies.

4.2 Impact of AGN driven shocks on the abundance profiles in galaxy clusters

. The large amount of metals, in particular - iron, observed in cool cluster cores is likely produced by stars in very bright galaxies (BCGs) dwelling in the centers of these clusters. The observed distribution of iron is, however, broader than the light distribution of the central galaxy. This suggests that the gas does not form a perfectly static atmosphere, but is instead involved in motions, that transport metals to larger radii. All cool core clusters contain a supermassive black hole (an AGN) in the BCG at the cluster center which is believed to be the source of energy for the cooling gas. In particular interesting is the example of a nearby Virgo cluster, where the central region around giant elliptical galaxy M87 has been recently studied in detail with the XMM-Newton and Chandra observatories.

Using simple 1D hydrodynamic model we evaluated the impact of gas shock heating by a central AGN in M87 on the radial distribution of heavy elements. The propagation of a shock creates an inverted entropy profile and the subsequent rearrangement of the gaseous atmosphere transports metal rich gas from the central region to larger radii. We show that for the parameters of the relatively weak shock, recently found in the gaseous atmosphere of M87, the abundance profile is not strongly affected by the redistribution of the shock heated gas (except for the very central region). At the same time, the energetics of the source is fully sufficient to broaden the metal distribution to match the observations, strongly suggesting that mechanisms other than direct shock heating must operate in cluster cores. The absence of a very strong abundance peak at the very center of M87 suggests that the central AGN produces frequent (every few 10 Myr) and relatively weak outbursts, rather than rarer (every few 100 Myr) and an order of magnitude more powerful events.